

The MUSIC of Galaxy Clusters I: Baryon properties and Scaling Relations of the thermal Sunyaev-Zel’dovich Effect

Federico Sembolini^{1,2*}, Gustavo Yepes¹, Marco De Petris², Stefan Gottlöber³,
Luca Lamagna², Barbara Comis²

¹*Departamento de Física Teórica, Módulo C-15, Facultad de Ciencias, Universidad Autónoma de Madrid, 28049 Cantoblanco, Madrid, Spain*

²*Dipartimento di Fisica, Sapienza Università di Roma, Piazzale Aldo Moro 5, 00185 Roma, Italy*

³*Leibniz-Institut für Astrophysik, An der Sternwarte 16, 14482 Potsdam, Germany*

Accepted XXXX . Received XXXX; in original form XXXX

ABSTRACT

We introduce the Marenstrum-MultiDark Simulations of galaxy Clusters (MUSIC) dataset. It constitutes one of the largest sample of hydrodynamically simulated galaxy clusters with more than 500 clusters and 2000 groups. The objects have been selected from two large N-body simulations and have been resimulated at high resolution using Smoothed Particle Hydrodynamics (SPH) together with relevant physical processes that include cooling, UV photoionization, star formation and different feedback processes associated to Supernovae explosions.

In this first paper we focus on the analysis of the baryon content (gas and star) of clusters in the MUSIC dataset both as a function of aperture radius and redshift. The results from our simulations are compared with a compilation of the most recent observational estimates of the gas fraction in galaxy clusters at different overdensity radii. We confirm, as in previous simulations, that the gas fraction is overestimated if radiative physics is not properly taken into account. On the other hand, when the effects of cooling and stellar feedbacks are included, the MUSIC clusters show a good agreement with the most recent observed gas fractions quoted in the literature. A clear dependence of the gas fractions with the total cluster mass is also evident. However, we do not find a significant evolution with redshift of the gas fractions at aperture radius corresponding to overdensities smaller than 1500 with respect to critical density. At smaller radii, the gas fraction do exhibit a decrease with redshift that is related the gas depletion due to star formation in the central region of the clusters. The impact of the aperture radius choice, when comparing integrated quantities at different redshifts, is tested. The standard, widely used definition of radius at a fixed overdensity with respect to critical density is compared with a definition of aperture radius based on the redshift dependent overdensity with respect to background matter density: we show that the latter definition is more successful in probing the same fraction of the virial radius at different redshifts, providing a more reliable derivation of the time evolution of integrated quantities. We also present in this paper a detailed analysis of the scaling relations of the thermal SZ (Sunyaev Zel’dovich) Effect derived from MUSIC clusters. The integrated SZ brightness, Y , is related to the cluster total mass, M , as well as, the $M - Y$ counterpart which is more suitable for observational applications. Both laws are consistent with predictions from the self-similar model, showing a very low scatter which is $\sigma_{\log Y} \simeq 0.04$ and even a smaller one ($\sigma_{\log M} \simeq 0.03$) for the inverse $M - Y$ relation. The effects of the gas fraction on the $Y - M$ scaling relation is also studied. At high overdensities, the dispersion of the gas fractions introduces non negligible deviation from self-similarity, which is directly related to the $f_{gas} - M$ relation. The presence of a possible redshift dependence on the $Y - M$ scaling relation is also explored. No significant evolution of the SZ relations is found at lower overdensities, regardless of the definition of overdensity used.

Key words: methods: N -body simulations – galaxies: clusters – galaxies: scaling relations – cosmology: theory – Sunyaev-Zel’dovich effect

arXiv:1207.4438v1 [astro-ph.CO] 18 Jul 2012

1 INTRODUCTION

Galaxy clusters are the biggest gravitationally bound objects of the Universe and constitute one of the best cosmological probes to measure the total matter content of the Universe. However, the total mass of these objects cannot be directly measured. It must be inferred from other observational quantities (X-ray or SZ Surface Brightness, Lensing distortions or number of galaxies). In all cases, one has to relate these quantities with the total mass of the system. Due to the complex physics involved in the processes of cluster formation, hydrodynamical numerical simulations have been a fundamental tool to calibrate mass proxies, define new ones, and to study the systematics affecting observational measurements. They are also indispensable to deeply study the formation and evolution of clusters of galaxies and all their gas-dynamical effects (Borgani & Kravtsov 2009).

The big progresses achieved in the last years by numerical simulations are well represented by their use to describe and to study X-ray temperatures and their relation with cluster gas mass (Ettori et al. 2004; Muanwong et al. 2006; Nagai et al. 2007a) as well as to compare numerical predictions with observed temperatures (Loken et al. 2002; Borgani et al. 2004; Leccardi & Molendi 2008), gas profiles (Roncarelli et al. 2006; Croston et al. 2008), or pressure profiles (Arnaud et al. 2010).

In an ideal scenario one would need to have a large sample of simulated galaxy clusters with enough numerical resolution (both in mass and in the gravity and pressure forces) to accurately resolve the internal substructures and with a detailed modelling of the most relevant physical processes. The best way to achieve this goal would be by simulating large cosmological boxes (Borgani et al. 2004; Gottlöber & Yepes 2007; Burns et al. 2008; Hartley et al. 2008; Boylan-Kolchin et al. 2009). Unfortunately, due to the large computational demand of these simulations, one needs to find a compromise between the three main ingredients: volume size, mass resolution and physical processes included. A possible solution to the computational problems related with scalability of the present-day hydro codes is to proceed, mimicking the observations, by creating a catalogue of resimulated galaxy clusters that are extracted from low resolution N-body simulations. The regions containing clusters of galaxies are then resimulated with very high resolution, adding only gas physics in the resimulated areas (Puchwein et al. 2008; Dolag et al. 2009; Lau et al. 2009; Fabjan et al. 2010). This so-called ‘zooming’ technique permits to simulate thousands of clusters basically independently from each other with less computational cost than a full box hydrodynamical simulation of the same resolution. By selecting all the objects formed in a given volume above a given mass threshold, mock volume limited sample catalogues can be generated and used in the study of the properties and interrelations of the different scaling laws of galaxy clusters. Following this procedure, we have generated the MUSIC (Marenostrum-MultiDark SImulation of galaxy Clusters) dataset, a large sample of simulated clusters of galaxies, composed of objects extracted from two large box cosmological simulations: the MareNostrum Universe and the MultiDark simulation. We selected all the clusters using criteria based on mass (selecting all the clusters having a total mass larger than $10^{15} h^{-1} M_{\odot}$) or on morphol-

ogy (selecting groups of clusters corresponding to different morphology classes, bullet-like clusters and relaxed clusters). All these objects have been resimulated with SPH particles, radiative physical processes and star formation prescriptions, improving by an order of magnitude the resolution with respect to the original simulations, as described in the next section. From this database, we will obtain mock observations for X-rays, SZ, lensing as well as optical galaxy counts. This will allow us to study the interrelations between the scaling laws associated to the different observables. In this paper we base our attention on the properties of the baryon content and the SZ effects and will leave a more detailed analyzes of the relations with the other observed properties for a further work.

In the last few decades the SZ effect (Sunyaev & Zeldovich 1970) has become one of the most powerful cosmological tool to study clusters of galaxies, as well as the nature of the dark matter and dark energy components of the Universe. The physical process of the SZ effect is the diffusion of CMB (Cosmic Microwave Background) photons with a hot plasma due to inverse Compton scattering. The thermal component of the SZ effect is largely enhanced by the presence of clusters of galaxies, the most massive bound objects in the Universe, where plasma is in hydrostatic equilibrium inside the gravitational potentials of dark matter. The Intra Cluster Medium (ICM) composed by high energy electrons constitutes an ideal laboratory to investigate the SZ effect. The brightness of the SZ effect turns out to be independent of the diffuser position, thus making it the best tool to find galaxy clusters at high redshift. Moreover, the SZ flux collected from the cluster region is proportional to the total thermal energy content, with a weak dependence on the complex physical processes acting at the inner regions (e.g. cooling flows, galaxy feedbacks etc) which mostly affect the X-ray luminosity. Therefore, these two properties: redshift independence and low scatter mass proxy makes the integrated Compton Y -parameter an efficient high- z mass-estimator.

Under the hypothesis that the evolution of galaxy clusters is driven mainly by gravitational processes (Kaiser 1986) and assuming hydrostatic equilibrium and an isothermal distribution of dark matter and ICM (Bryan & Norman 1998) it is possible to derive simple scaling power-laws linking cluster properties: the so-called self-similar scaling relations. In the case of SZ science, the relation linking the SZ brightness with the cluster total mass, the $Y - M$ scaling law, is continuously under analysis to test for its robustness, allowing the application of the SZ effect as a mass-finder.

Observational studies started to collect data of a few clusters, mostly those with high X-ray luminosities (and therefore high masses) (Benson et al. 2004; Morandi et al. 2007; Bonamente et al. 2008; Vikhlinin et al. 2009; Arnaud et al. 2010). Recent large surveys have shown the possibility of detecting undiscovered clusters only through SZ effect observations, as in the claims by South Pole Telescope (SPT, Staniszewski et al. 2009; Vanderlinde et al. 2010; Andersson & SPT Collaboration 2010); Williamson et al. 2011), Atacama Cosmology Telescope (ACT, Marriage et al. 2011; Sehgal et al. 2011) and Planck (Planck Collaboration et al. 2011a; Planck Collaboration et al. 2011c; Planck Collaboration et al. 2011b; Planck Collaboration et al. 2011d). The possibilities to explore more distant objects or to deeply map single cluster morphology are planned with the ongoing higher angular resolution projects like AMI (Zwart et al. 2008), AMiBA (Lo et al. 2001), MUSTANG (Korngut et al. 2011), OCRA (Browne et al. 2000), CARMA (Muchovje et al. 2012) or the in-coming projects like the ground based C-CAT (Golwala et al. 2007), the upgraded with new spectroscopic capabilities MITO (De Petris et al. 2007) and the balloon-borne

* E-mail: federico.sembolini@uam.es

OLIMPO (Masi et al. 2008) or the proposed satellite mission *Millimetre* (<http://www.sron.rug.nl/millimetre>).

More recent blind-surveys carried out by SPT, ACT and Planck enlarged the existing dataset confirming the self-similarity in the sample at least for the massive clusters (Marriage et al. 2011; Andersson et al. 2011; Planck Collaboration et al. 2011b). Numerical simulations have shown that Y (the integral of the Compton y -parameter over the solid angle of the cluster) is a good mass proxy (da Silva et al. 2004; Motl et al. 2005; Aghanim et al. 2009) and that the slope and the evolution of SZ scaling relations are apparently not affected by redshift evolution and cluster physics. In order to find an X-ray equivalent of the SZ integrated flux, the numerical simulations also led to the introduction of a new mass proxy: the Y_X parameter, defined as the product of the cluster gas mass and its temperature (Kravtsov et al. 2006).

Many works based on large N -body cosmological simulations have already studied the impact of gas physics on SZ scaling relations (da Silva et al. 2000; White et al. 2002; da Silva et al. 2004; Motl et al. 2005; Nagai 2006; Bonaldi et al. 2007; Hallman et al. 2007; Aghanim et al. 2009; Battaglia et al. 2011; Kay et al. 2012), such as the effects introduced by clusters with disturbed morphologies (Poole et al. 2007; Wik et al. 2008; Yang et al. 2010; Krause et al. 2012), showing that the self-similar model is valid at least up to cluster scales (even if with some differences introduced by the different models used in the simulations).

In what follows, we will present an analysis of the relation between the SZ integrated flux and the total mass, Y - M , in MUSIC clusters and will compare it with the predictions of the self-similar model. We also study the possible biases introduced by the common assumption of considering quantities (M or Y) integrated inside a radius defined by a fixed overdensity with respect to the critical density instead of a more suitable definition with respect to the background density whose value depends on redshift.

We will focus our analysis of the Y - M scaling relation on the most massive objects of the MUSIC dataset which constitutes an almost complete volume limited sample. Therefore, only clusters with virial masses $M_v > 5 \times 10^{14} h^{-1} M_\odot$, are considered in this paper. We will extend our analysis to a wider range of masses in an upcoming work.

The paper is organized as follows. In Section 2 the MUSIC database is described. The baryon content in the clusters at different overdensities is presented in Section 3, together with a study of its evolution with redshift and a comparison of our numerical results with the most recent observational estimates. In Section 4 the Y - M scaling relation is computed from the MUSIC clusters and compared with the predictions from the self-similar model. We also discuss the validity of the integrated Y as a proxy for the cluster mass. In Section 5 we focus on the impact of the gas fraction on the Y - M relation together with the dependence of the gas fraction on the cluster mass. Finally in Section 6 the redshift evolution of the Y - M relation is discussed. In Section 7 we summarize and discuss our main results.

2 THE MUSIC DATASET

The MUSIC project consists of two sets of resimulated clusters extracted from two large volume simulations:

- *The MareNostrum Universe*, a non-radiative SPH simulation with 2 billion particles ($2 \times 10^{14} h^{-1}$ gas and dark matter) in a $500 h^{-1}$ Mpc cubic box (Gottlöber & Yepes 2007).

- *The MultiDark Simulation*, a dark-matter only N-body simulation with 2048^3 particles in a $1 h^{-1}$ Gpc cubic box (Prada et al. 2011).

These two simulations have slightly different cosmologies. The MareNostrum Universe (MU) was made with the cosmological parameters that were compatible with WMAP1 results ($\Omega_M=0.3$, $\Omega_b=0.045$, $\Omega_\Lambda=0.7$, $\sigma_8=0.9$, $n=1.0$, $h=0.7$) while the MultiDark run was done using the best-fit cosmological parameters to WMAP7 + BAO + SNI ($\Omega_M=0.27$, $\Omega_b=0.0469$, $\Omega_\Lambda=0.73$, $\sigma_8=0.82$, $n=0.95$, $h=0.7$) (Komatsu et al. 2011).

The procedure to select the interested objects in those two simulations was also different. For the MareNostrum clusters we mainly selected them based on the dynamical state (relaxed vs bullet-like clusters). For the MultiDark clusters we made a mass limited selection, taking all clusters with masses above $10^{15} h^{-1} M_\odot$ at $z=0$.

The zooming technique (Klypin et al. 2001) was used to produce the initial conditions of the resimulated objects. Namely, we first found all particles within a sphere of 6 Mpc radius around the center of each selected object at $z=0$ from a low resolution version (256^3 particles) of the two simulations. This set of particles was then mapped back to the initial conditions to find out the Lagrangian region corresponding to a $6 h^{-1}$ Mpc radius sphere centred at the cluster centre of mass at $z=0$. The initial conditions of the original simulations were generated in a finer mesh of 2048^3 (for the MareNostrum) and 4096^3 (for the MultiDark) sizes. Therefore, we could improve the mass resolution of the resimulated objects by a factor of 8 with respect to the original simulations. We kept the highest mass-refinement level within the Lagrangian region of each cluster and then cover it with shells of increasing mass particles down to the lower resolution level of 256^3 . To avoid problems with periodic conditions, we always recentre the simulations, each resimulated cluster always located at the center of the corresponding box. Thus, for the MultiDark clusters, we have dark matter particles of 5 different mass refinements (from 4096^3 to 256^3) while for the MareNostrum clusters we have 4 different mass species. The gas SPH particles were added only to the highest refinement level. The SPH particle positions were slightly displaced from their parent dark matter by 0.4 times the mean inter particle distance in the 3 spatial directions and they were given the same initial velocity as their dark matter counterparts.

The parallel TreePM+SPH GADGET code (Springel 2005) was used to run all the resimulations. We accounted for the effects of radiative cooling, UV photoionization, star formation and supernova feedback, including the effects of strong winds from supernova, in the same way as described in Springel & Hernquist (2003) model. We refer the reader to this reference for a detailed description of the model. Here we simply provide the values corresponding to the typical parameters of the model. Stars are assumed to form from cold gas clouds on a characteristic timescale t_* and a certain stellar mass fraction β is instantaneously released due to supernovae from massive stars ($M > 8 M_\odot$). We adopt a fraction of $\beta=0.1$ which is consistent with assuming an Universal Salpeter IMF with a slope of -1.35 in the limits of $0.1 M_\odot$ and $40 M_\odot$. In addition to this mass injection of hot gas, thermal energy is also released to the ISM by the supernovae. This feedback energy heats the ambient gas and cold clouds can be evaporated inside hot bubbles of supernovae. All these assumptions lead to a self-regulating star formation, where the growth of cold clouds is balanced by supernova feedback of the formed stars. The number of collision-less star particles spawned from one SPH parent gas particle is fixed to

2, which means that each stellar particle will get half of the original parent SPH mass. In addition to the thermal feedback, some sort of kinetic feedback is also accounted for. Gas mass losses due to galactic winds, \dot{M}_w , is assumed to be proportional to the star formation rate M_{SFR} , i.e. $\dot{M}_w = \eta M_{\text{SFR}}$ with $\eta=2$. Additionally, the wind contains a fixed fraction ϵ of the total supernova energy, which is assumed to be $\epsilon = 0.5$. SPH particles near the star formation region will be subject to enter in the wind in a stochastic way. Those particles eligible for winds will be given an isotropic velocity kick of $v=400$ km/s and will freely travel without feeling pressure forces up to 20 kpc distance from their original positions.

Using the aforementioned techniques we have been able to resimulate a total of 700 different galaxy clusters from the two large box simulations. This constitutes one of the largest samples of resimulated cluster-sized objects. We used two different selection criteria, based on dynamical state and on mass cuts in order to explore scaling relations dependencies on different aspects (mass, morphology, redshift evolution, overdensity). All these clusters were also resimulated with non-radiative physics, using only SPH and gravity forces, so we can also account for the effects of cooling, star formation and supernovae feedbacks on the observed properties of the clusters.

The database of MUSIC clusters is publicly available in a SQL query format through the website: <http://music.ft.uam.es>. The database will comprehend also the initial conditions of all MUSIC objects, in order to give the possibility to resimulate the clusters with other hydro codes and/or with different modelling for the radiative processes (e.g. AGN feedback, MHD, Cosmic ray pressure, etc).

In what follows we describe in more detail the two main subsamples in which the MUSIC database is divided.

2.1 MUSIC-1: MareNostrum resimulated clusters

This first subset is composed of 164 resimulated clusters extracted from the MU.

There are more than 4000 clusters of galaxies (objects larger than $10^{14} h^{-1} M_\odot$) in the whole MU simulation. Out of this large number of clusters, we selected 82 'bullet-like' clusters. The 1ES0657-556 cluster (Clowe et al. 2006), generally known as the bullet cluster, is considered one of the best astrophysical tools to study the nature of dark matter. This cluster, located at $z = 0.296$, is composed by a smaller merger which has just crossed a bigger object and is now moving away. The core of the plasma cloud of the merging sub-cluster, 'the bullet', has survived the passage. Due to the different dynamics of the collision less dark matter component and the x-ray emitting gas, it is expected that the two components have a spatial offset. By combining lensing and X-ray observations, this behaviour is seen explicitly in the bullet cluster. The relative velocity of the two merging systems is a quantity that is not directly measured. It is derived from the shape of the "bow shock" clearly seen in X-ray images, using the results from different hydro simulations of merger clusters (Springel & Farrar 2007; Mastropietro & Burkert 2008). But a more direct measure of the effects of a cluster merger, in the gas and dark matter components, is the projected 2D separation between the peak of the two distributions (gas and dark matter). Forero-Romero et al. (2010) have used this measurement to characterize the number of bullet-like clusters in the MU. They define a "bullet" cluster if the 2D separation between the peak of dark matter and the peak of gas distribution is at least 200 kpc (as in the real bullet cluster).

In order to have a morphological counterpart to these ex-

tremely disturbed systems, we also selected another 82 clusters which exhibit the following relaxed conditions: the displacement between dark and baryonic matter is smaller than 200 kpc and they are composed of a single massive cluster with no big substructures (i.e. all substructures inside the virial radius must have masses smaller than 10 per cent of the total mass).

The relaxed clusters were chosen to have masses similar to those of the bullet systems: in this way every bullet-like cluster has a relaxed companion of the same mass. All the selected clusters were resimulated using the zooming technique and radiative physics, including radiative cooling, heating processes of the gas arisen from a UV background, star formation and supernovae feedback explained above. The particle mass of dark matter was set to $m_{DM}=1.03 \times 10^9 h^{-1} M_\odot$ and the mass of SPH gas particle to $m_{gas}=1.82 \times 10^8 h^{-1} M_\odot$. Due to the relative small size of the computational box of the MU simulation, very few clusters of MUSIC-1 subset have a mass at the virial radius bigger than $10^{15} h^{-1} M_\odot$. The cluster masses of MUSIC-1 span from $M_v=2 \times 10^{15} h^{-1} M_\odot$ to $M_v=1 \times 10^{14} h^{-1} M_\odot$.

2.2 MUSIC-2 : MultiDark resimulated clusters

The second, and more numerous, subset of MUSIC consists of a mass limited sample of resimulated clusters selected from the MultiDark Simulation (MD). This simulation is dark-matter only and contains 2048^3 (almost 9 billion) particles in a $(1h^{-1}\text{Gpc})^3$ cube. It was performed in 2010 using ART (Kravtsov et al. 1997) at the NASA Ames Research centre. All the data of this simulation are accessible from the online *MultiDark Database* (www.MultiDark.org). We have selected, using a low resolution (256^3 particles) version of the MD simulation, all the objects more massive than $10^{15} h^{-1} M_\odot$. In total, we found 282 objects above this mass limit. All these massive clusters were resimulated both with and without radiative physics using the techniques explained above. The mass resolution for these simulations corresponds to $m_{DM}=9.01 \times 10^8 h^{-1} M_\odot$ and to $m_{SPH}=1.9 \times 10^8 h^{-1} M_\odot$. The gravitational softening was set to $6 h^{-1}$ kpc for the SPH and dark matter particles in the high-resolution areas. Several low mass clusters have been found close to the large ones and not overlapping with them. Thus, the total number of resimulated objects is considerably larger. In total we obtained 535 clusters with $M > 10^{14} h^{-1} M_\odot$ at $z = 0$ and more than 2000 group-like objects with masses in the range $10^{13} h^{-1} M_\odot < M_v < 10^{14} h^{-1} M_\odot$. All of these resimulations have been done both with non-radiative physics, using the same technique and resolutions as the radiative ones.

We have stored snapshots for 15 different redshifts in the range $0 \leq z \leq 9$ for each resimulated object. In the case of the two massive clusters, we stored 320 snapshots for a more detailed study of the formation process. A graphical representation of the gas distribution for all the MUSIC-2 clusters for each of the 15 redshifts in radiative and non-radiative runs can be seen online at <http://music.ft.uam.es>. In Fig.1 we show, as an example, the gas density, colour coded according to the temperature, and the stellar component for 4 different clusters of the MUSIC database at $z = 0$.

The cumulative mass function of MUSIC-2 clusters in the redshift range $0 \leq z \leq 1$ is shown in figure 2. The mass values of the dataset completeness for all redshifts analyzed are shown in Table 1, spanning from $4.5 \times 10^{14} h^{-1} M_\odot$ at $z=1$ to $8.5 \times 10^{14} h^{-1} M_\odot$ at $z = 0$.

In this first paper about MUSIC clusters, we focused our analysis only on the most massive objects of MUSIC-2, selecting all the

z	0.00	0.11	0.25	0.33	0.43	0.67	1.00
M_v	8.5	7.5	7.5	7.0	7.0	4.5	4.5
N	172	147	90	76	41	57	14

Table 1. Mass completeness of MUSIC-2 dataset (compared to dark-matter only MD simulation) in the redshift range $0 \leq z \leq 1$. The virial mass is reported in $10^{14} h^{-1} M_\odot$ and N is the number of clusters beyond the completeness mass limit.

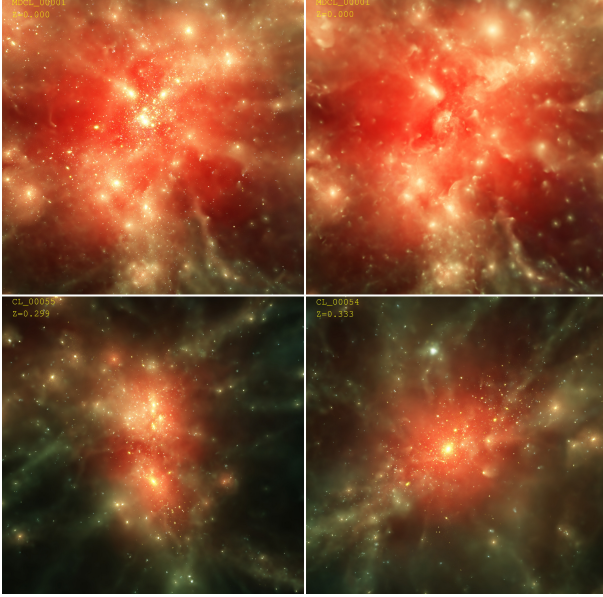


Figure 1. Gas distribution in MUSIC clusters: the physics at $z = 0$; a bullet-like cluster (bottom-left) and a relaxed cluster (bottom-right) of MUSIC-1 at $z = 0.3$. The images of the all MUSIC dataset (available at <http://music.ft.uam.es>) have been generated with SPLOTCH (Dolag et al. 2008).

clusters of the dataset, both radiative (CSF) and non-radiative (NR), with virial mass $M_v > 5 \times 10^{14} h^{-1} M_\odot$ at $z = 0$. This selection allows us to analyze a subset in a mass range where MUSIC constitutes a complete volume limited sample (more than 80 per cent of the clusters found in the $1 h^{-1} \text{Gpc}$ MD box above this mass limit have been resimulated by MUSIC). Moreover, those clusters are the best resolved ones, containing millions of particles. This allows us to extend the analysis towards the inner regions of the clusters. The selected subset has been analyzed at seven different redshifts. In Table 1, we show the actual redshifts analyzed and the total number of clusters used in each redshift bin. We did not include any of the MUSIC-1 clusters in this analysis, as only very few of them have a virial mass larger than $5 \times 10^{14} h^{-1} M_\odot$ at $z = 0$.

2.3 Halo-finding and general properties of the clusters

Halo and sub-halo of MUSIC simulations have been identified and their properties have been measured using the hybrid MPI+OpenMP parallel halo finder AHF (see Knollmann & Knebe 2009 for a detailed description), a code whose algorithm automatically identifies haloes, sub-haloes, sub-subhaloes, etc.

It has been proven that it can reliably recover substructures containing at least 20 particles (Knebe et al. 2011).

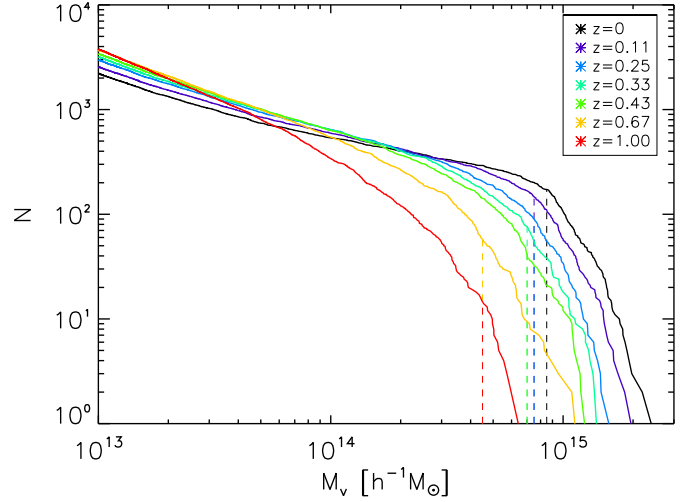


Figure 2. Cumulative mass function of the MUSIC-2 dataset from $z = 0$ to $z = 1$. The vertical lines indicate the mass limit beyond which the dataset constitutes a complete volume limited sample

The luminosity of the stars formed in the simulation has been computed using the STARDUST (Devriendt et al. 1999) code, a stellar population synthesis model of the spectral energy distributions (SEDs) of star bursts from far-UV to radio wavelengths. From the SEDs of the stars we could compute the total luminosity in different photometric bands for each object of the simulation.

Simulated X-rays maps of our clusters will be produced using X-MAS (Gardini et al. 2004; Rasia et al. 2008) and PHOX (Biffi et al. 2012), tools developed in order to simulate X-ray observations of galaxy clusters obtained from hydrodynamical N -body simulations. One of the main characteristics of these codes is to generate event files following the same standards used for real observations, allowing to analyze simulated observations with the same tools of real observations.

Here, we provide the estimated X-ray temperatures of the simulated clusters as:

$$T_{mw} = \frac{\sum_i T_i m_i}{\sum_i m_i} \quad (1)$$

$$T_{ew} = \frac{\sum_i m_i \rho_i \Lambda(T_i) T_i}{\sum_i m_i \rho_i \Lambda(T_i)} \quad (2)$$

$$T_{sl} = \frac{\sum_i \rho_i m_i T_i^{1/4}}{\sum_i \rho_i m_i T_i^{-3/4}} \quad (3)$$

calculating the mass weighted temperature (Eq.1), the emission weighted temperature (Eq.2) and the spectroscopic-like temperature (Eq.3) (Mazzotta et al. 2004), where m_i , ρ_i , T_i are the gas particle mass, density and electronic temperature and $\Lambda(T)$ is the cooling function. The particle gas densities of the CSF runs have been corrected in order to take into account the multiphase model adopted in the radiative simulation; the spectroscopic-like and emission-weighted temperatures have been calculated only by considering gas particles with $kT > 0.5 \text{ keV}$ and we have assumed $\Lambda(T) \propto \sqrt{T}$ corresponding to thermal bremsstrahlung. For all the MUSIC-2 objects (clusters and groups) the three temperature definitions, estimated at the virial radius, are shown in Fig. 3 along with the corresponding virial mass, M_v , at $z = 0$ for both the simulations (NR and CSF). We will have a more detailed analysis of the cluster X-ray properties in a following papers.

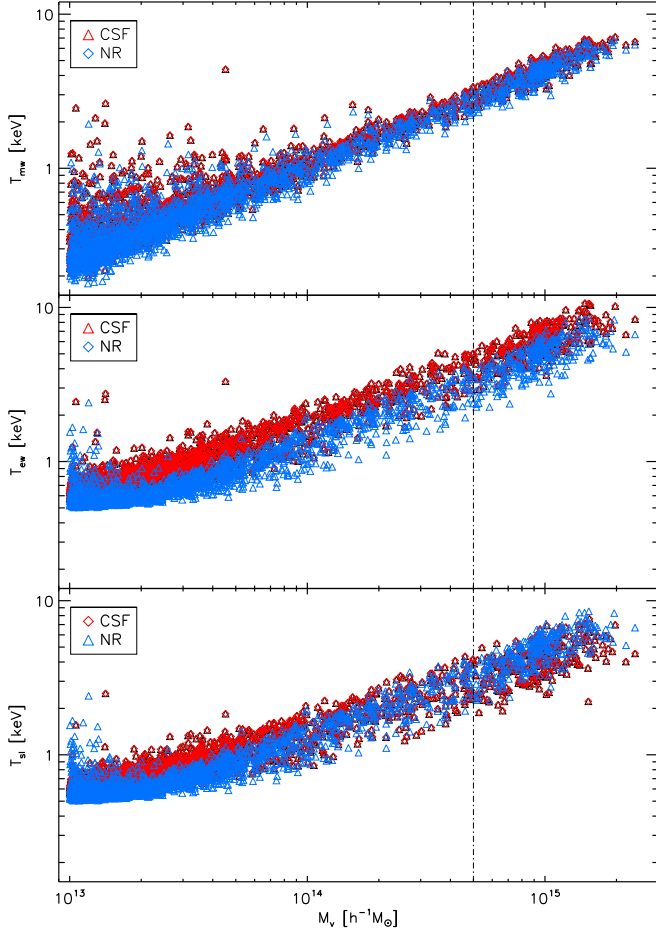


Figure 3. Distribution of mass-weighted (top panel), emission-weighted (middle panel) and spectroscopic-like (bottom panel) temperatures of all MUSIC-2 objects (clusters and groups) at virial radius as a function of the virial mass at $z = 0$. Red diamonds refer to CSF objects, blue triangles to NR objects. The dashed vertical line indicates the subset analyzed in this paper ($M_v > 5 \times 10^{14} h^{-1} M_\odot$ at $z = 0$).

3 BARYON CONTENT OF MUSIC-2 MASSIVE CLUSTERS

We study the internal baryon content of the MUSIC-2 cluster sample estimating the gas and stellar fractions, as well as the total baryon fraction. In this way we are able to check the consistency between our simulated dataset and available observational results. Moreover, as examined in the following section, the gas fraction plays a relevant role on the $Y - M$ scaling relation. The over cooling effect, a hot topic in all cluster simulations (Kravtsov et al. 2005), is also monitored in this dataset.

The mass of each component is estimated inside fixed overdensity radii defined either with respect to the critical or background density. In both cases, we calculate the gas mass $M_{gas,\Delta}$, the star mass $M_{star,\Delta}$ and the total mass M_Δ inside a fixed overdensity radius r_Δ selecting and summing all the particles of gas, star and dark matter falling inside that radius. We then define the

baryon, gas and star fractions as:

$$f_{gas} = \frac{M_{gas,\Delta}}{M_\Delta} \quad (4)$$

$$f_{star} = \frac{M_{star,\Delta}}{M_\Delta} \quad (5)$$

$$f_{bar} = \frac{M_{gas,\Delta} + M_{star,\Delta}}{M_\Delta} \quad (6)$$

These quantities are calculated for the CSF clusters. In the case of the NR simulations, where all the SPH particles are gas, only the baryon fraction, defined as $f_{bar} = M_{gas,\Delta}/M_\Delta$ is estimated.

From now on, we are going to compare the integrated cluster properties at different redshifts. It is therefore very important the definition of the aperture radius where the properties are estimated. The most often used, more favourable in terms of simplicity, consists on defining the radius at which the mean enclosed total density is a fixed factor (independent on redshift) of the critical density of the Universe, $\rho_c(z)$. This is useful to make comparisons with theoretical predictions from the spherical collapse model, which describe the virialized part of a cluster in terms of the density contrast Δ_v . But Δ_v varies with redshift and depends on the cosmological parameters adopted. Thus, as we show in Appendix A, this definition of aperture radius based on the same critical overdensity value at different redshift does not allow to consider a region of the clusters corresponding to the same fraction of the virial radius, $R_v(z)$ at different redshift. This could introduce a bias in the study of the redshift evolution of integrated cluster quantities simply due to the different cluster regions probed at different redshifts. To alleviate this problem, it is useful to adopt another definition of aperture radius based on the redshift-dependent background density, $\rho_b(z)$. This approach was introduced the first time by Maughan et al. (2006) to study the evolution of cluster X-ray scaling relations, but it has never been considered in the study of the SZ relations before. In this paper we use both definitions of aperture radii: a fixed value, independent on redshift, critical overdensity and a redshift-dependent background overdensity. We refer the reader to Appendix A in which we compare the redshift evolution of the radii for these two definitions.

In order to have a detailed description of the integrated cluster properties starting from the inner regions up to the virial radius, we analyze our clusters at seven different critical overdensities, $\Delta_c = [\Delta_{v,c}(z), 200, 500, 1000, 1500, 2000, 2500]$, where only the virial value is different for each redshift as in Eq.(A6). Similarly we select a set of (redshift dependent) background overdensities, $\Delta_b(z) = [\Delta_{v,b}(z), 500(z), 1000(z), 1500(z), 2500(z), 5000(z), 7000(z)]$, where we are adopting the notation used by Maughan et al. (2006). We are referring to an overdensity $\Delta_b(z)$ corresponding to the value at $z = 0$ but that is changing its value along the redshift (i.e. writing $7000(z)$ it means that we assume $\Delta_b = 7000$ at $z = 0$ and varying the value with redshift as in Eq.(A8)). These values have been chosen aiming at having the same fraction of the clusters volume than those analyzed with a fixed critical overdensity criteria. In this way we can infer the properties at overdensities corresponding to cluster regions that are well fitted by X-ray observations or by current SZ observations. Due to the high resolution of our simulations, we can extend the analysis down to the cluster innermost regions ($\Delta_c = 2500$). Overdensities higher than 2500, corresponding to the core region of the cluster, can be affected in a non negligible way by cold flows or galaxy feedbacks.

Fig.4 shows the evolution of the gas, star and baryonic fractions in a region close to the cluster centre, ($\Delta_b = 7000(z)$)

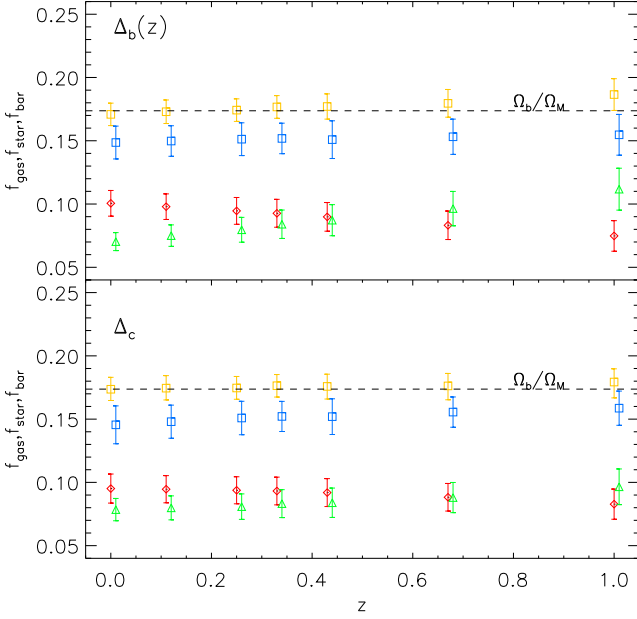


Figure 4. Evolution of f_{gas} (red diamonds), f_{star} (green triangles) and f_{bar} (yellow squares) of CSF clusters and f_{bar} (blue squares) of NR clusters for $\Delta_b=7000(z)$ (top panel) and $\Delta_c=2500$ (bottom panel).

and $\Delta_c=2500$), corresponding at almost $R_v/5$. When we consider $\Delta_c=2500$ we observe a moderate decrease in the gas fraction as we go from $z = 0$ ($f_{gas}=0.09\pm0.01$) to $z = 1$ ($f_{gas}=0.08\pm0.01$). Correspondingly, the value of the star fraction grows from $f_{star}=0.08\pm0.01$ at $z = 0$ to $f_{star}=0.10\pm0.01$ at $z = 1$. The baryon fraction shows, however, no significant variation with redshift, and it is compatible with the cosmic value $\Omega_b/\Omega_m=0.174$ (Komatsu et al. 2011) for CSF clusters ($f_{bar}=0.174\pm0.009$), while it is smaller for NR clusters ($f_{bar}=0.15\pm0.01$). We find a similar scenario when we define the aperture radius based on $\Delta_b=7000(z)$, but in this case the evolution of gas and star fraction with redshift is more evident: from $f_{gas}=0.09\pm0.01$ and $f_{star}=0.07\pm0.01$ at $z = 0$ to $f_{gas}=0.07\pm0.01$ and $f_{star}=0.11\pm0.02$ at $z = 1$. We observe that at these overdensities the value of the star fraction is high, especially at high redshifts, but the effects of a possible over cooling in our simulations do not seem to be strong enough to deviate the mean values of the gas fraction from the observational estimates.

The evolution of the same baryonic component fractions is shown in Fig. 5 but for a larger integration domain defined by an overdensity: $\Delta_b = 1500(z)$ and $\Delta_c = 500$ respectively, corresponding to $\sim R_v/2$. In this case there are neither any relevant differences between the two overdensities used to define the radii, nor there is a significant evolution with redshift observed. Therefore, we can confidently assume the values at $z = 0$ for $\Delta_c=500$ to be representative (within 10%) of the gas fraction values for clusters up to $z = 1$: $f_{gas}=0.118\pm0.005$, $f_{star}=0.048\pm0.003$, $f_{bar}=0.166\pm0.004$. For NR clusters we have $f_{bar}=0.157\pm0.006$.

Fig. 6 shows the average radial (normalized to the virial radius) cluster profiles of gas, star and baryonic fractions for all the redshift considered in this analysis. An evolution of the baryon properties with redshift is clearly seen in this plot, which is more relevant at smaller R/R_v . The gas fraction increases from inner to outer regions and shows higher values at low redshifts. On the con-

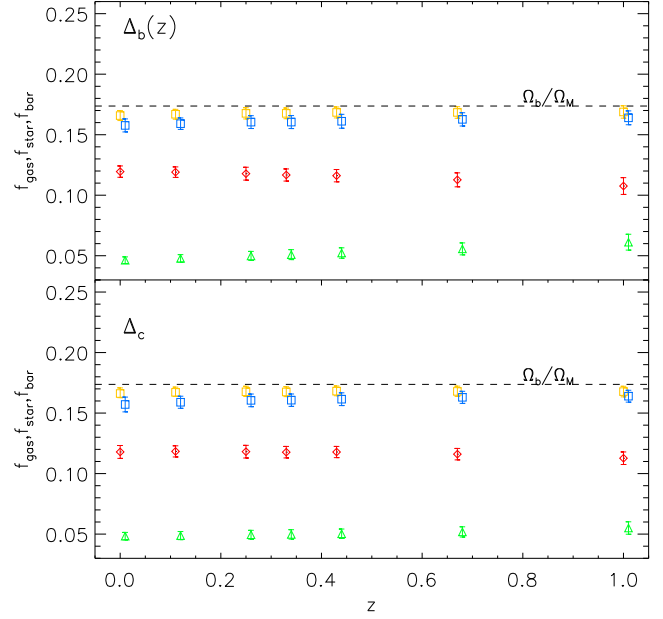


Figure 5. Evolution of f_{gas} (red diamonds), f_{star} (green triangles) and f_{bar} (yellow squares) of CSF clusters and f_{bar} of NR clusters (blue squares) for $\Delta_b=1500(z)$ (top panel) and $\Delta_c=500$ (bottom panel).

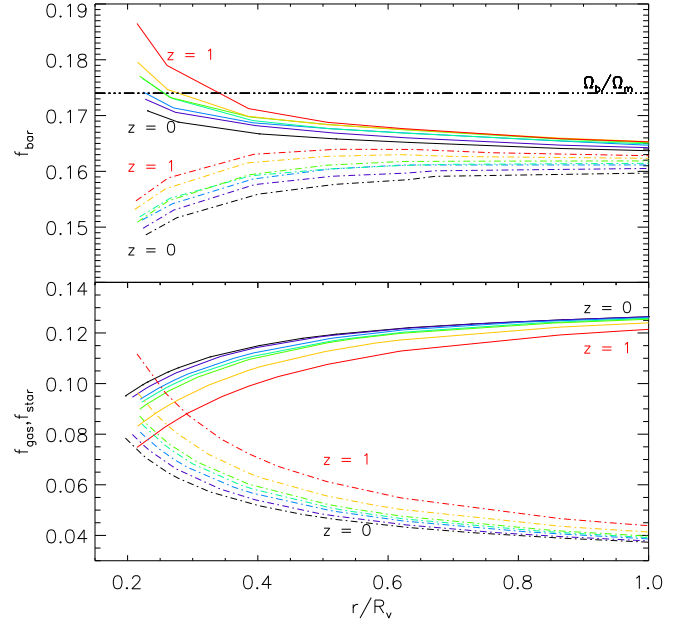


Figure 6. Top panel: Average radial profiles, in units of the virial radius, of f_{bar} for CSF clusters (continuous lines) and for NR cluster (dashed) at different redshifts from $z=0$ (black) to $z=1$ (red). Bottom panel: f_{gas} (continuous lines) and f_{star} (dashed lines) profiles for CSF clusters only, from $z = 0$ (black) to $z = 1$ (red).

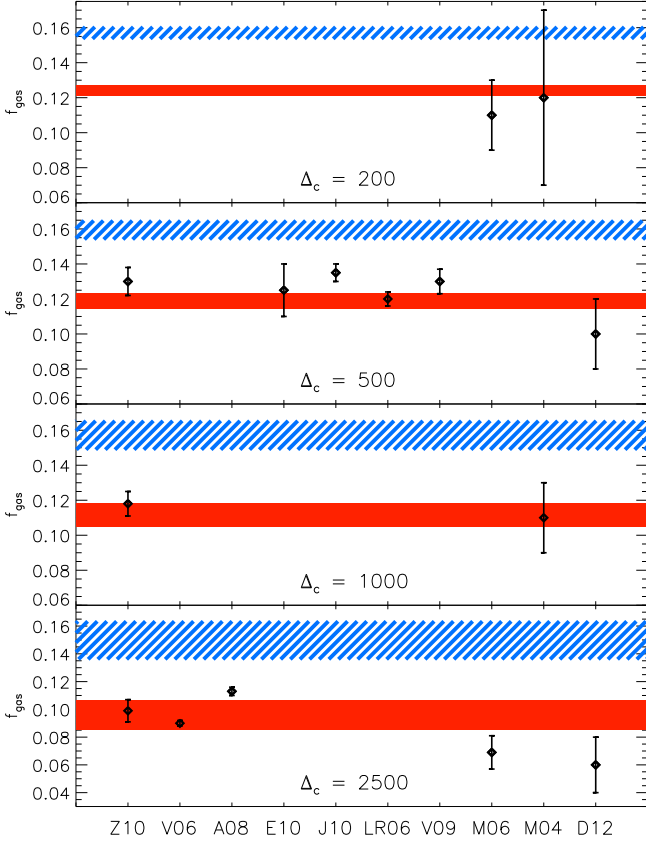


Figure 7. Comparison among gas fractions of MUSIC-2 clusters at different overdensities and observational estimates. Blue dashed area shows the 1σ dispersion of f_{gas} derived from the volume limited NR MUSIC-2 clusters while the red solid area corresponds to the CSF MUSIC-2 clusters. The x -axis denotes the different observations: Z10 (Zhang et al. 2010), V06 (Vikhlinin et al. 2006), A08 (Allen et al. 2008), E10 (Ettori et al. 2009), J10 (Juett et al. 2010), LR06, (LaRoque et al. 2006), V09 (Vikhlinin et al. 2009), D12 (David et al. 2012), M04 (Maughan et al. 2004), M06 (Maughan et al. 2006).

trary, the star fraction decreases when moving towards the virial radius and is bigger at higher redshifts, showing that star formation is preferentially located at the central parts of clusters at low redshift. The baryon fraction decreases when reaching the cluster outskirts for CSF clusters (with mean values higher than the cosmic ratio) while the NR clusters show the opposite behaviour. In both physical configurations the mean baryon fraction becomes smaller when moving from $z = 1$ to $z = 0$. The evolution of f_{bar} at large fractions of the virial radius is very mild for CSF clusters and converges towards a nearly constant gas fraction for $\Delta_c = 500$.

As a summary of the previous discussion we conclude that using $\Delta_b(z)$ to define the aperture radius at different redshift allows to reliably compare the same region (with respect to the virial radius of the cluster at each redshift) and thus is the best choice when studying redshift evolutions. On the other hand, by selecting the radius based on fixed Δ_c values allows us to use a f_{gas} which is nearly constant with redshift.

We now compare the values of the gas fractions derived from our simulations with those measured in observations.

In Fig.7 we show a compilation of published f_{gas} estimates from observations at different overdensities and our numerical re-

sults for the corresponding overdensities, both from the NR and CSF MUSIC clusters within the 1σ dispersion values.

Our results are consistent with the gas fractions that have been measured at 3 overdensities ($\Delta_c = 2500, 1000, 500$) by the LoCuSS project (Zhang et al. 2010). At $\Delta_c = 500$ we also found consistency with f_{gas} estimated by Ettori et al. (2009), Juett et al. (2010), LaRoque et al. (2006), Vikhlinin et al. (2009), Maughan et al. (2006), Maughan et al. (2004) and David et al. (2012).

At $\Delta_c=2500$ our results are still consistent with Vikhlinin et al. (2006) and Maughan et al. (2006), while Allen et al. (2008) shows a higher value of the gas fraction.

At $\Delta_c=200$ our clusters are also compatible with the two only measurements at these large radius, Maughan et al. (2006), Maughan et al. (2004), but due to the larger error bars they are less restrictive.

4 SZ CLUSTER SCALING RELATIONS

The correlation of the SZ signal with other cluster properties was initially studied by considering the central comptonization parameter, y_0 , (see Cooray et al. 1999 and McCarthy et al. 2003) but the inadequacy of a simple β -model for the ICM spatial distribution was in short clear. For the first time Benson et al. (2004) applied the Compton y -parameter integrated within a redshift-independent density contrast, $\Delta_c=2500$, in a SZ scaling relation for 15 clusters observed with SuZIE II. As the y_0 parameter gives only local information about the status of the cluster, the integrated Y constitutes a global property, strongly bound to the energy of the cluster (Mroczkowski et al. 2009) and less model-dependent.

The comparison between quantities integrated within a constant critical overdensity is now widely employed in X-ray and SZ scaling relations analysis at overdensities $\Delta_c=2500$ (Comis et al. 2011; Bonamente et al. 2008) and $\Delta_c = 500$ (Arnaud et al. 2010; Planck Collaboration et al. 2011c, Andersson et al. 2011). The great benefit, distinctive in SZ observations of ignoring cluster redshift to correct the redshift dependence of the overdensity, is evident.

In order to give an estimate of the integrated Y of MUSIC clusters, we have produced simulated maps of the thermal SZ effect, integrating along the projected radius to extract the value of Y at fixed redshift and overdensity.

4.1 Cluster y -map generation

The maps of the Compton y -parameter are generated with the implemented procedure employed in Flores-Cacho et al. (2009). The simulation provides for each i -th SPH particle: position (\mathbf{r}_i), velocity (\mathbf{v}_i), density (ρ_i), internal energy (U_i) and SPH smoothing length (h_i). In CSF simulations we also find the number of ionized electrons per hydrogen particle ($N_{e,i}$) and metallicity Z_i : using this additional information we could achieve a more detailed estimate of electron temperature T_e (per gas particle) as:

$$T_e = (\gamma - 1) U m_p \frac{\mu}{k_B} \quad (7)$$

where m_p is the proton mass, γ the polytropic coefficient (set to 5/3 for monatomic gases) and μ the mean molecular weight of electrons, that we estimate as

$$\mu = \frac{1 - 4Y_{He}}{1 + \gamma + N_e} \quad (8)$$

(Y_{He} is the nuclear helium concentration). The number electron density (in cm^{-3}) is derived as

$$n_e = N_e \rho_{gas} \left(\frac{1 - Z - Y_{He}}{m_p} \right) \quad (9)$$

(The density ρ_{gas} of the gas particles of CSF particles has been corrected in order to take into account the multiphase model adopted in the simulation)

We are interested only in the thermal component of the SZ effect. This is quantified in the Compton y -parameter:

$$y = \int n_e \frac{k_B T_e}{m_e c^2} \sigma_T dl \quad (10)$$

The integral can be discretized along the line of sight (los) as

$$y \simeq \frac{k_B \sigma_T}{m_e c^2} \sum_i n_{e,i} T_{e,i} W_p(|\mathbf{r}_i - \mathbf{r}_{com}|, h_i), \quad (11)$$

where the tSZ signal associated to each particle is spread to the surrounding area by the mass profile $m_{gas} W_p(|\mathbf{r}_i - \mathbf{r}_{com}|, h_i)$, where W_p is the projection of the normalized spherically symmetric spline kernel W used in the simulations:

$$W(x, h_i) = \frac{8}{\pi h_i^3} \begin{cases} 1 - 6x^2 + 6x^3, & 0 \leq x \leq 0.5 \\ 2(1-x)^3, & 0.5 \leq x \leq 1 \\ 0, & x > 1 \end{cases} \quad (12)$$

4.2 SZE scaling relations

The integrated Compton y -parameter, Y , appears to be a very good cluster mass proxy. With the aim to properly employ SZ observations as mass finder, it is fundamental to accurately calibrate the $Y - M$ scaling relation.

As the integrated Compton parameter Y is a very good proxy of the clusters mass, it is fundamental to study the Y - M scaling relation. The Y parameter is estimated as follows:

$$Y \equiv \int_{\Omega} y d\Omega = D_A^{-1} \left(\frac{k_B \sigma_T}{m_e c^2} \right) \int_0^{\infty} dl \int_A n_e T_e dA \quad (13)$$

where D_A is the angular distance and the integration is performed inside the solid angle, Ω , equal to an area A in the projected map, corresponding to an overdensity Δ .

Adopting a self-similar model to describe clusters of galaxies (assuming hydrostatic equilibrium and isothermal distribution for dark matter and gas particles) the gas temperature is related to the mass by a simple power law:

$$T_e \propto (M_{\Delta} E(z))^{2/3} \quad (14)$$

where, as we said in the previous section, the total mass is calculated inside the overdensity radius r_{Δ} we are considering and $E(z)$ the Hubble constant normalized to its present day value defined as $E(z) = (\Omega_M(1+z)^3 + \Omega_{\Lambda} + \Omega_k(1+z)^2)^{1/2}$. Due to the hypothesis of isothermal equilibrium, Y is proportional to the integral of the electron density n_e over a cylindrical volume, leading to:

$$Y_C D_A^2 \propto T_e \int n_e dV \propto M_{gas} T_e = f_{gas} M_{tot} T_e \quad (15)$$

Considering Eq.(14), we find a relation that depends directly on M_{tot} and f_{gas} :

$$Y_C D_A^2 \propto f_{gas} M_{tot}^{5/3} E(z)^{2/3} \quad (16)$$

To fit a spherical quantity, like the total energy of a cluster, it is

better to introduce the spherical integrated Y_S parameter. This is defined as the Compton- y parameter integrated inside a spherical volume with a radius equal to r_{Δ} . The Eq.(16) turns out to be:

$$Y_{S,\Delta} = \frac{\sigma_T}{m_e c^2} \frac{\mu}{\mu_e} \left(\frac{\sqrt{\Delta_c} G H_0}{4} \right)^{2/3} E(z)^{2/3} f_{gas,\Delta} M_{tot,\Delta}^{5/3} \quad (17)$$

where with $Y_{S,\Delta}$ we denote the Y parameter integrated over a cluster centred sphere of radius r_{Δ} . Here, we are assuming a constant f_{gas} independent on the cluster mass for each overdensity. We calculate from the map the Y_{Δ} parameter at the considered overdensity integrating along all the pixels of the projected map falling inside the projected radius r_{Δ} :

$$Y_{S,\Delta} = \sum_{i,r < r_{\Delta}} y_i \times dl_{pix}^2 \quad (18)$$

In order to take into account the different integration domain, we define the C parameter as:

$$C = \frac{Y_C D_A^2}{Y_S} \quad (19)$$

In Fig 8 we give an estimate of C from the values of Y_S and $Y_C D_A^2$ computed from our clusters at different redshifts and overdensities. We find that C is constant with redshift and grows with overdensity. Available values in literature are consistent with ours: at $\Delta_c=2500$ we found $C=2.0 \pm 0.5$, in agreement with the estimate of $C \simeq 2$ given by Bonamente et al. (2008) and $C=1.67 \pm 0.80$ given by Comis et al. (2011), while at $\Delta_c=500$ we have $C=1.3 \pm 0.2$, compatible with Andersson et al. (2011). From now on we will denote the spherical Y_S parameter simply as Y .

The $Y - M$ scaling relation at a fixed overdensity is studied performing a best fit of

$$Y_{\Delta} = 10^B \left(\frac{M_{\Delta}}{h^{-1} M_{\odot}} \right)^A E(z)^{2/3} [h^{-2} Mpc^2] \quad (20)$$

where M_{Δ} is the total mass calculated inside the sphere of radius r_{Δ} that we are considering and B the normalization, defined as:

$$B = \log \frac{\sigma_T}{m_e c^2} \frac{\mu}{\mu_e} \left(\frac{\sqrt{\Delta_c} G H_0}{4} \right)^{2/3} + \log f_{gas}, \quad (21)$$

contains all the constant terms of the first part of the right hand of Eq.(17). We remind that, if the clusters follow the self-similar model, then the slope A is expected to be $5/3$.

We are also interested in the inverse scaling relation $M - Y$, which is more easily applicable to observational clusters (the mass should be inferred from Y measurements):

$$M_{\Delta} = 10^{B*} \left(\frac{Y_{\Delta}}{h^{-2} Mpc^2} \right)^{A*} E(z)^{-2/5} [h^{-1} M_{\odot}] \quad (22)$$

We study these scaling relations in the log-log space, in the form $\log Y = B + A \log X$, where in the case of the $Y - M$ relation we have $X = M$ and $Y = Y E(z)^{\kappa} f_{gas}^{-1}$: κ is fixed to its expected self-similar scaling with z ($\kappa = -2/3$) and in this case f_{gas} is not included in the normalization parameter B .

Figure 9 shows the $Y - M$ scaling relation of our dataset at $\Delta_c = 500$ for both physical configurations. We choose to consider a value of f_{gas} constant at fixed overdensity and redshift, assigning to all clusters the mean value of f_{gas} as:

$$f_{gas}(\Delta, z) = \sum_{i=1}^N \frac{f_{gas,i}(\Delta, z)}{N} \quad (23)$$

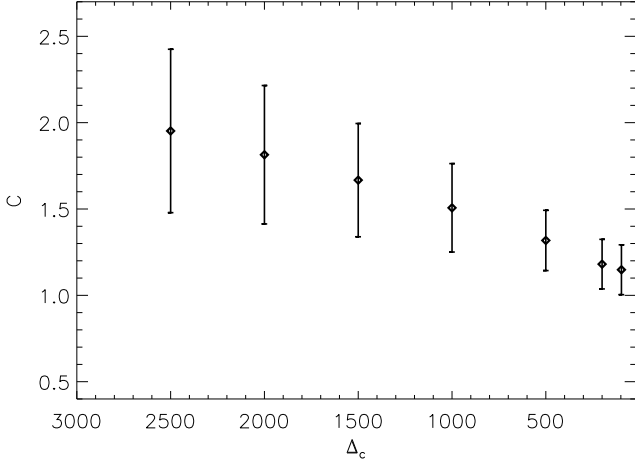


Figure 8. Behavior of the $C=Y_C D_A^2/Y_S$ parameter with critical overdensity: each value corresponds to the mean value calculated over all the redshifts analyzed. The error bars represent the mean error calculated from the mean values of C over all redshifts.

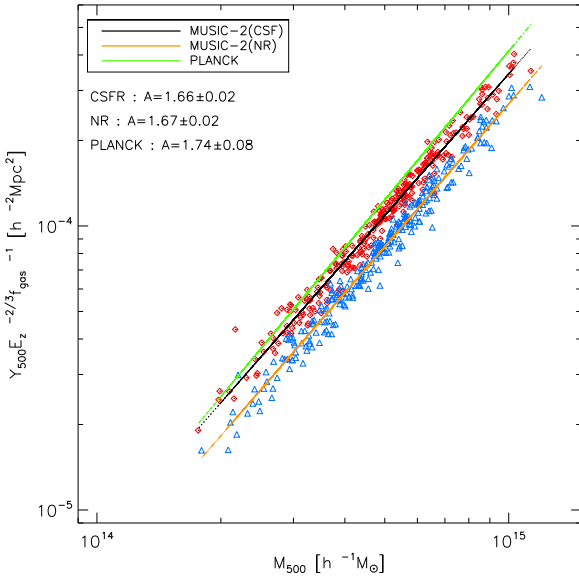


Figure 9. $Y-M$ scaling relation at $z=0$, $\Delta_c=500$. CSF clusters are shown as red diamonds (the best fit as a black solid line) and NR as blue triangles (best fit as an orange solid line). The green line shows the best fit from Planck data after the removal of the positive bias in the X-ray mass estimates with respect to weak lensing masses (see text).

where N is the number of clusters in the considered subset.

CSF clusters show higher values than NR clusters, as the relation depends on the inverse of f_{gas} , which is bigger for NR clusters, (see Section 3).

The values of A and B at $z=0$ with their $1-\sigma$ errors are listed in Table 2 and shown in Fig. 10. At all the overdensities considered, the values of the slope A seem to agree, within their errors, with the self-similar prediction of $5/3$. NR clusters seem to show a lower slope at high overdensities and CSF clusters an higher one, matching both with the same self-similar value at $\Delta_c=500$. The value of B seems to stay almost constant at all overdensities.

Leaving aside a possible variation with redshift, which is stud-

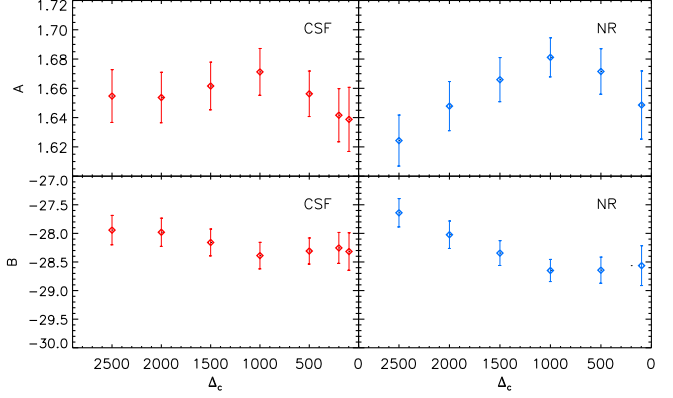


Figure 10. The best-fit slope A (top panels) and normalization B (bottom panels) of the $Y-M$ scaling relation as a function of overdensity for $z=0$ CSF (left panel) and NR (right panel) MUSIC-2 clusters.

ied in section 6, we can therefore express the $Y-M$ scaling relation at $\Delta_c=500$ as:

$$Y_{500} = 10^{-28.3 \pm 0.2} \left(\frac{M_{500}}{h^{-1} M_{\odot}} \right)^{1.66 \pm 0.02} E(z)^{2/3} [h^{-2} Mpc^2] \quad (24)$$

We estimate the scatter on the $Y-M$ relation by computing the sum of the residuals as follows:

$$\sigma_{\log_{10} Y} = \sqrt{\frac{\sum_{i=1}^N [\log Y_{\Delta,i} - (A \log M_{\Delta,i} + B)]^2}{N-2}} \quad (25)$$

As shown in Table 2, the scatter on the Y estimate is about 5 per cent at all overdensities.

In the same way we also calculate the $M-Y$ scaling relation. Fig. 11 shows the relation at $z=0$ for $\Delta_c=500$, for which the self-similar model predicts a slope $A^*=3/5$. Table 2 also lists the best fit values of A^* at $z=0$, which seem to be rather independent on overdensity and to agree within the errors with the self-similar prediction. In Fig. 12 we show the evolution of A^* and B^* with overdensity. We can then express the best-fit $M-Y$ scaling relation at $\Delta_c=500$ as:

$$M_{500} = 10^{17.0 \pm 0.1} \left(\frac{Y_{500}}{h^{-2} Mpc^2} \right)^{0.59 \pm 0.01} E(z)^{-2/5} [h^{-1} M_{\odot}] \quad (26)$$

Moreover, the $M-Y$ relation seems to show a smaller scatter (3 per cent) than the $Y-M$. The difference between the two relations is shown in Fig. 13, in which we show the distribution of the residuals at $\Delta_c=500$. Both distributions are well fitted by a Gaussian with zero mean and different widths. The distributions of residuals for the $M-Y$ is narrower (i.e. smaller σ) than the corresponding one for $Y-M$.

Therefore, we can establish that the MUSIC-2 clusters show $Y-M$ and $M-Y$ scaling relations that are well consistent with the self-similar model both at high and low overdensities. This result confirms, if necessary, the validity of the self-similar model in using the integrated Y parameter as a proxy of the mass and, at the same time, demonstrates the reliability of the MUSIC cluster dataset for the study of scaling relations. No significant discrepancies can be pointed out between the two relations, $Y-M$ and $M-Y$. Therefore we will focus all further analyzes described in the next sections only on the first one.

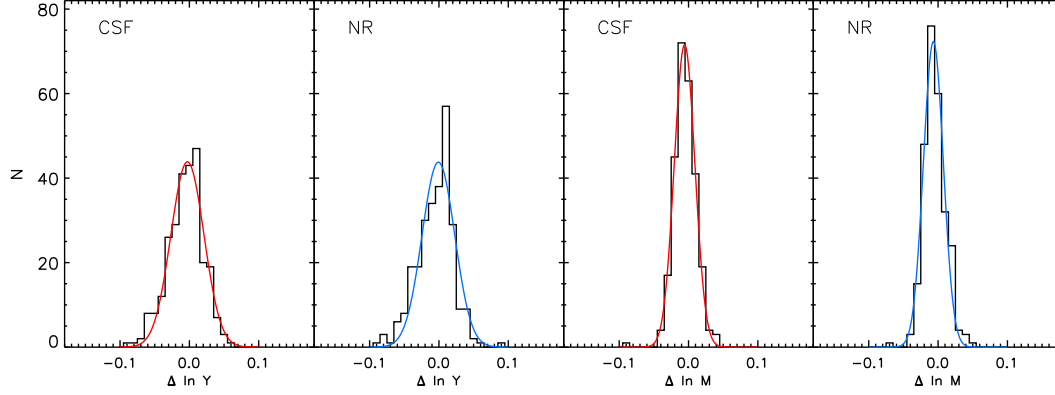


Figure 13. Distribution of the residuals of the $Y - M$ (in $\log Y$, left panels) and $M - Y$ (in $\log M$, right panels) scaling relations at $z = 0$ for $\Delta_c = 500$. The red (CSF) and blue (NR) lines represent the best fit Gaussian curves to the residual distribution.

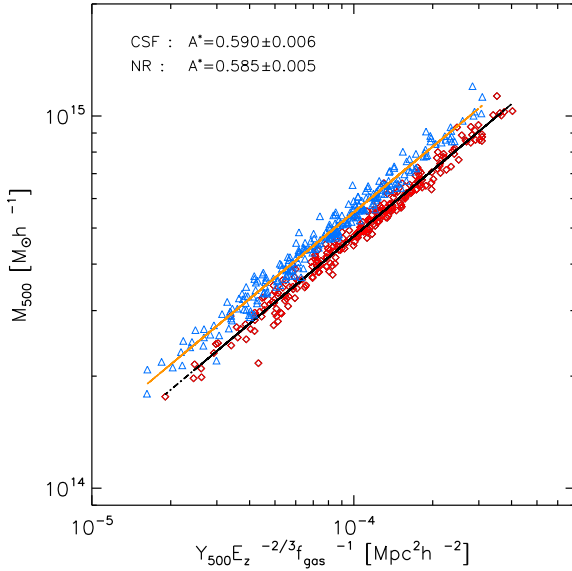


Figure 11. $M - Y$ scaling relation at $z = 0$ for $\Delta_c = 500$: CSF clusters are shown as red diamonds (the best fit as a black line) and NR as blue triangles (best fit as an orange line).

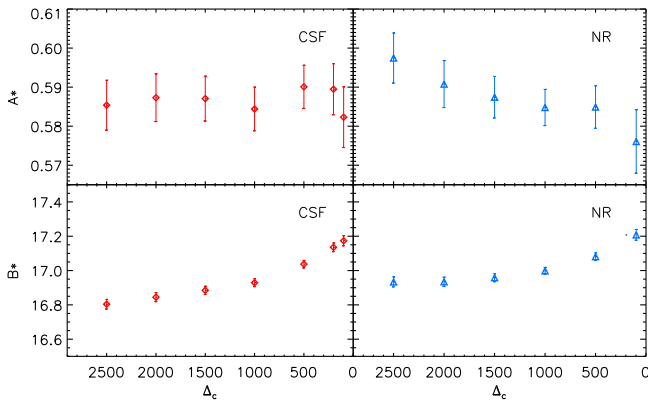


Figure 12. Same as Fig 10 but for the $M - Y$ scaling relation.

4.3 Comparison with observations

Several scaling-laws have been derived from different SZ observations (Bonamente et al. 2008; Andersson & SPT Collaboration 2010; Arnaud et al. 2010; Comis et al. 2011; Planck Collaboration et al. 2011b; Andersson et al. 2011). Here, our numerical results are compared with the best fit scaling relation $Y_{500} - M_{500}$ based on 62 nearby clusters detected at high signal-to-noise in the first Planck all-sky data set (Planck Collaboration et al. 2011c). We have taken into account the 22 ± 8 per cent mass overestimation of the X-ray Planck cluster masses derived from the comparison with weak lensing mass estimates (Planck Collaboration et al. 2012). This discrepancy can be attributed to the errors in the mass concentration measurements and to an offset in the cluster centres between X-rays and lensing observations. Correcting the Planck scaling relation by this factor, we find a very good agreement, at $\Delta_c = 500$, with the scaling relation of MUSIC-2 CSF clusters, as can be seen in Fig.9.

The masses assigned to the MUSIC clusters are of course free of systematic errors since they are the true masses computed from the simulations. We have checked how the numerical SZ scaling relation would be affected if we assume the hypothesis of hydrostatic equilibrium (HSE), to derive the mass of the clusters, as is usually done in observations. The HSE assumption constitutes one of the most significant uncertainties in the derivation of the observational scaling relations. We calculate the HSE cluster mass at a given overdensity as:

$$M_{HSE,\Delta}(< r) = -\frac{kTr}{G\mu m_H} \left(\frac{d \ln \rho}{d \ln r} + \frac{d \ln T}{d \ln r} \right) \quad (27)$$

We used the mass weighted temperature profile of the gas using Eq.(1) to calculate the gas particle temperature. Although the spectroscopic like-temperature would have been more fitted to compare with X-ray observations, we do not expect that the conclusions could be significantly different. The distribution of the Hydrostatic Mass Bias (HMB), quantified as $\Delta M = (M_{500,HSE} - M_{500})/M_{500}$, can be seen in Fig. 14. A systematic underestimation of 25 per cent of the true mass by using the hydrostatic mass is found, with a dispersion of $\sigma = 0.43$. The result is consistent with recent numerical simulations that also find that the HSE assumption underestimates the true mass up to 20 per cent (Rasia et al. 2006; Kay et al. 2007; Nagai et al. 2007a; Nagai et al. 2007b; Piffaretti & Valdarnini 2008; Ameglio et al. 2009; Lau et al. 2009). A more detailed analysis of the HMB, especially at high overdensity regions where a significant

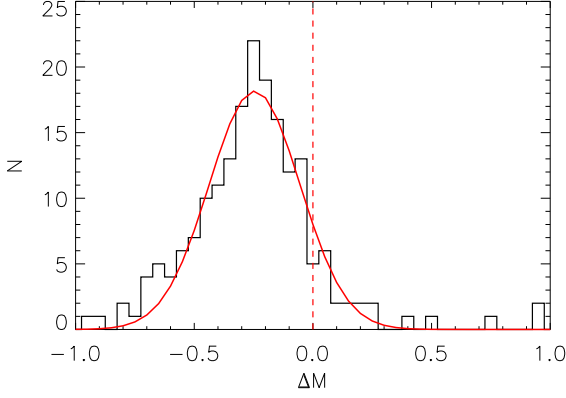


Figure 14. Distribution of the hydrostatic mass bias of M_{500} for CSF clusters at $z = 0$. The red curve represents the Gaussian curve which best fits the distribution. The Gaussian is centered at $\Delta M = -0.25$ with a width of $\sigma = 0.43$.

contribution from non-thermal pressure is present even in relaxed clusters, is under way and it will be the topic of a further paper.

5 THE EFFECT OF THE GAS FRACTION ON THE Y-M SCALING RELATIONS

In the previous section we assumed a constant gas fraction for all clusters used to fit the $Y - M$ scaling law at a given redshift and overdensity. This assumption is a common observational approach in scaling laws study due to the large uncertainty occurring in single cluster measurements. In numerical simulations we can easily estimate the gas fraction of each single object and investigate in more detail its impact on the $Y - M$ scaling relation.

In this section we leave the value of f_{gas} free. Therefore, using Eq.(20) we can derive the modified scaling relation:

$$Y_{\Delta} f_{gas}^{-1} = 10^{B_1} \left(\frac{M_{\Delta}}{h^{-1} M_{\odot}} \right)^{A_1} E(z)^{2/3} [h^{-2} Mpc^2] \quad (28)$$

In Table 3 we present the best fit values of the $Y f_{gas}^{-1} - M$ relation at $z = 0$, for overdensities in the range $\Delta_c = 2500$ to $\Delta_{v,c}$. We note that the slope is steeper and the normalization is larger (in absolute value) than the $Y - M$ with fixed f_{gas} , as can be seen in Fig. 15, and the distribution of residuals is wider and less regular (Fig.16). Since we saw before that $Y - M$ agrees very well with the self-similar predictions, it follows that the departure from self similarity can be attributed to the dependence of f_{gas} on the cluster total mass. This effect seems to be independent on redshift but very sensitive on the overdensity value: core regions present a larger deviation from the self-similar values than halo outskirts.

We now study the relation between $f_{gas} - M$ in the form:

$$f_{gas} = 10^{B_2} \left(\frac{M_{\Delta_c}}{h^{-1} M_{\odot}} \right)^{A_2} \quad (29)$$

It can be easily deduced that introducing the above mass dependence f_{gas} into the $Y - M$ scaling relation is equivalent to splitting Eq. 20 into two expressions described by Eq.(28) and Eq.(29), whose best-fit parameters are connected by the simple relation:

$$A = A_1 + A_2 \quad (30)$$

$$B = B_1 + B_2 \quad (31)$$

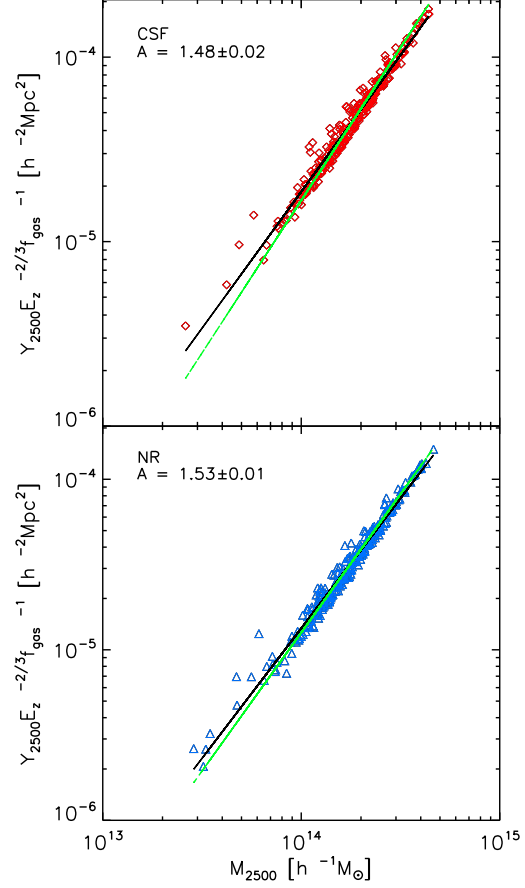


Figure 15. $Y f_{gas} - M$ scaling relation at $z = 0$, $\Delta_c = 2500$ for CSF clusters (top panel) and NR clusters (bottom panel). The black line shows the best-fit relation, the green line the best-fit relation of the $Y - M$ scaling relation (with constant f_{gas}).

Since we are dealing with massive clusters, we expect a linear relation (in the log space) between the gas fraction and the total mass (Vikhlinin et al. 2009). In Fig. 17 we represent the results for the $f_{gas} - M$ from our MUSIC clusters for two different overdensities. As can be seen in this figure and in Table 3, the relation is steeper at the central parts of the clusters and it is shallower in the outskirts while the scatter also increases towards the centre. To test for the effects of cooling and star formation in this and other scaling relations, we always compare them with the results from the non radiative simulations of the same clusters. We see from Fig. 17 and Table 3) that a similar dependence on mass is also present in NR clusters, although somewhat shallower than in the case of CSF clusters.

We can therefore express the best-fit gas fraction dependence on mass at $\Delta_c = 500$ as:

$$f_{gas} = 10^{-1.6 \pm 0.1} \left(\frac{M_{500}}{h^{-1} M_{\odot}} \right)^{0.04 \pm 0.01} \quad (32)$$

As we said, this relation becomes much less steep at high overdensities, where the $f_{gas} - M$ scaling relation at $\Delta_c = 2500$ can be written as:

$$f_{gas} = 10^{-3.5 \pm 0.2} \left(\frac{M_{2500}}{h^{-1} M_{\odot}} \right)^{0.17 \pm 0.01} \quad (33)$$

In Figs. 18 and 19 we represent the evolution with redshift of

	Δ_c	2500	2000	1500	1000	500	200	98v
CSF								
$Y - M$	A	1.65 ± 0.02	1.65 ± 0.02	1.66 ± 0.02	1.67 ± 0.02	1.66 ± 0.02	1.64 ± 0.02	1.64 ± 0.02
	B	-27.9 ± 0.3	-28.0 ± 0.2	-28.2 ± 0.2	-28.4 ± 0.2	-28.3 ± 0.2	-28.3 ± 0.2	-28.3 ± 0.3
	$\sigma_{\log Y}$	0.05	0.05	0.05	0.04	0.04	0.04	0.05
$M - Y$	A*	0.585 ± 0.006	0.587 ± 0.006	0.587 ± 0.006	0.584 ± 0.006	0.590 ± 0.005	0.589 ± 0.007	0.582 ± 0.008
	B*	16.8 ± 0.03	16.8 ± 0.02	16.9 ± 0.02	16.9 ± 0.02	17.0 ± 0.02	17.1 ± 0.02	17.2 ± 0.03
	$\sigma_{\log M}$	0.03	0.03	0.03	0.03	0.02	0.03	0.03
NR								
$Y - M$	A	1.62 ± 0.02	1.65 ± 0.02	1.67 ± 0.02	1.68 ± 0.02	1.67 ± 0.02	1.66 ± 0.02	1.65 ± 0.02
	B	-27.6 ± 0.2	-28.0 ± 0.2	-28.3 ± 0.2	-28.6 ± 0.2	-28.6 ± 0.2	-28.3 ± 0.2	-28.5 ± 0.3
	$\sigma_{\log Y}$	0.06	0.05	0.04	0.04	0.04	0.04	0.05
$M - Y$	A*	0.597 ± 0.006	0.591 ± 0.006	0.587 ± 0.005	0.585 ± 0.005	0.585 ± 0.005	0.598 ± 0.006	0.576 ± 0.008
	B*	16.9 ± 0.03	16.9 ± 0.02	17.0 ± 0.02	17.0 ± 0.02	17.1 ± 0.02	17.2 ± 0.02	17.2 ± 0.03
	$\sigma_{\log M}$	0.03	0.03	0.03	0.02	0.02	0.02	0.03

Table 2. Best fit slope, normalization and scatter of $Y - M$ (A, B, $\sigma_{\log Y}$) and $M - Y$ (A*, B*, $\sigma_{\log M}$) scaling relations for CSF and NR clusters.

	Δ_c	2500	2000	1500	1000	500	200	98v
CSF								
$Y - M_{gas}$	A1	1.48 ± 0.02	1.51 ± 0.01	1.55 ± 0.01	1.59 ± 0.01	1.61 ± 0.01	1.62 ± 0.01	1.63 ± 0.02
	B1	-25.5 ± 0.2	-25.9 ± 0.2	-26.5 ± 0.2	-27.2 ± 0.2	-27.7 ± 0.2	-28.0 ± 0.2	-28.2 ± 0.3
$f_{gas} - M$	A2	0.17 ± 0.01	0.15 ± 0.01	0.11 ± 0.01	0.08 ± 0.01	0.04 ± 0.01	0.02 ± 0.01	0.01 ± 0.01
	B2	-3.5 ± 0.2	-3.1 ± 0.2	-2.6 ± 0.2	-2.2 ± 0.1	-1.6 ± 0.1	-1.2 ± 0.1	-1.0 ± 0.1
NR								
$Y - M_{gas}$	A1	1.52 ± 0.01	1.56 ± 0.01	1.59 ± 0.01	1.63 ± 0.01	1.66 ± 0.01	1.66 ± 0.01	1.65 ± 0.01
	B1	-26.2 ± 0.02	-26.8 ± 0.02	-27.3 ± 0.02	-27.9 ± 0.01	-28.4 ± 0.01	-28.5 ± 0.01	-28.6 ± 0.01
$f_{gas} - M$	A2	0.10 ± 0.01	0.09 ± 0.01	0.07 ± 0.01	0.05 ± 0.01	0.02 ± 0.01	-0.03 ± 0.01	-0.04 ± 0.01
	B2	-2.2 ± 0.2	-2.1 ± 0.2	-1.9 ± 0.2	-1.6 ± 0.1	-1.0 ± 0.1	-0.8 ± 0.1	-0.7 ± 0.1

Table 3. Best fit slope, normalization and scatter of $Y f_{gas} - M$ (A1,B1) and $f_{gas} - M$ (A2, B2) scaling relations for CSF and NR clusters.

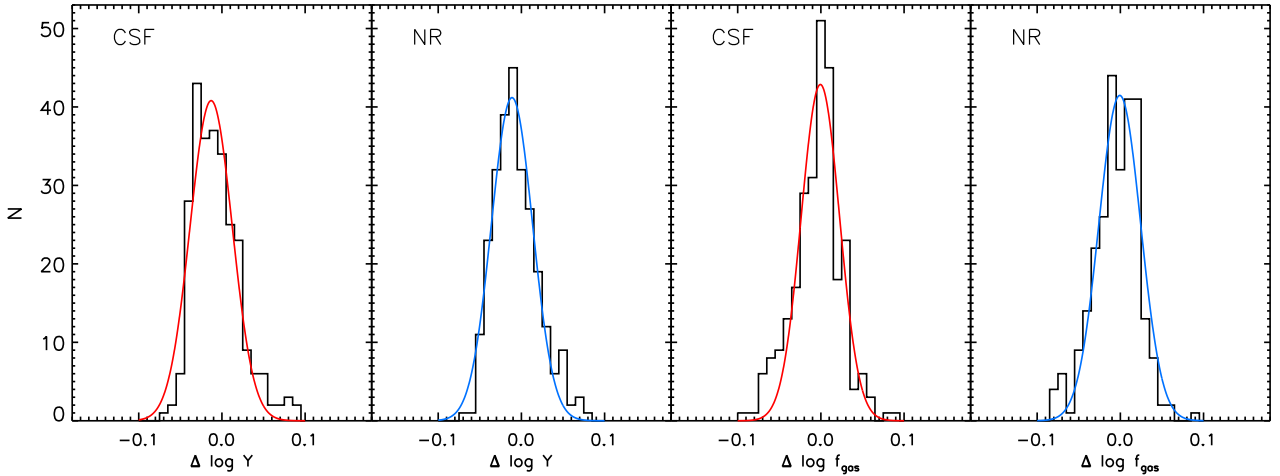


Figure 16. left panel: the distribution of residuals for $Y f_{gas} - M$ at $z = 0$ and $\Delta_c=2500$. Right panel: same as left panel but for the $f_{gas} - M$ scaling relation. The red (CSF) and blue (NR) lines represent the Gaussian curves which best fit the residual distribution.

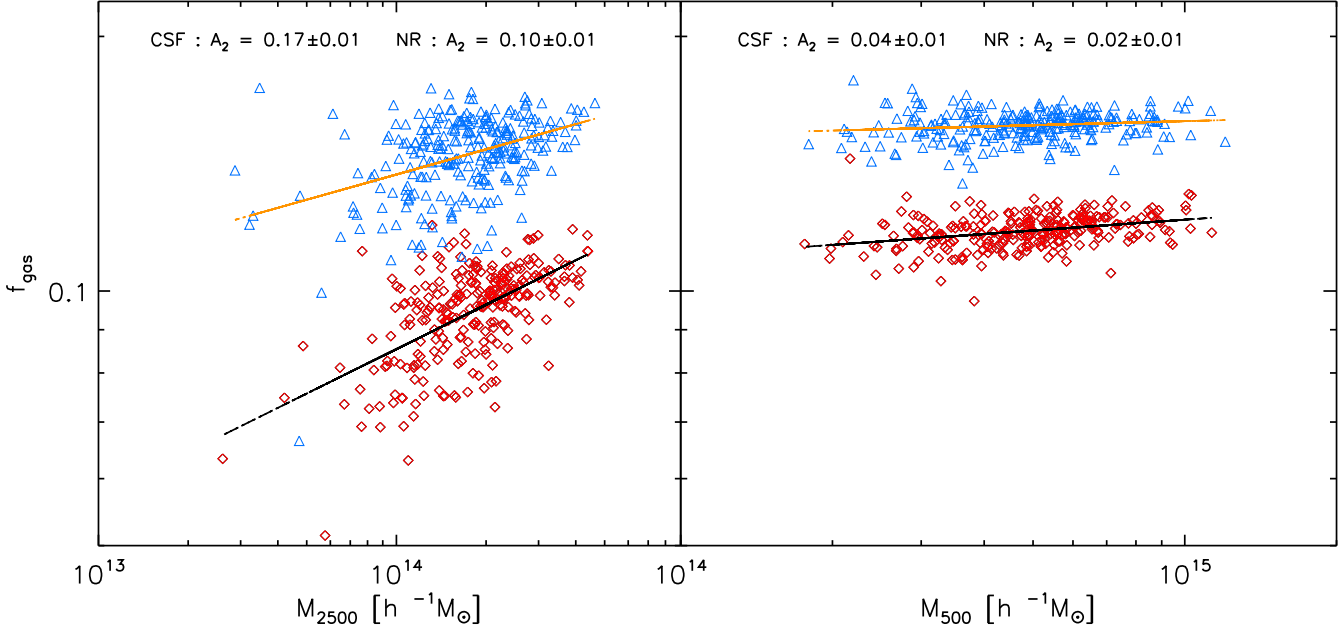


Figure 17. The $f_{gas} - M$ scaling relation at $z = 0$ for $\Delta_c = 2500$ (left panels) and $\Delta_c = 500$ (right panels). CSF clusters are shown in red diamonds, NR clusters in blue triangles. The values of the slope A_2 are also reported in the label.

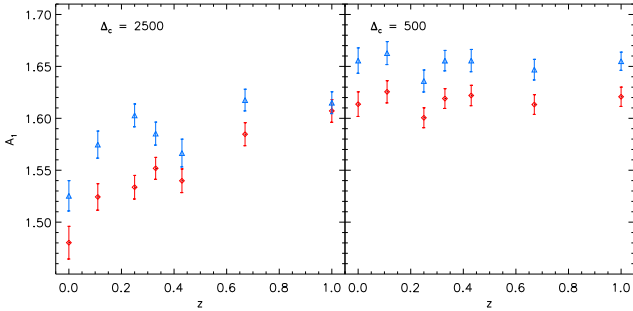


Figure 18. Evolution of the A_1 slope parameter of the $Y f_{gas}^{-1} - M$ scaling relation at $\Delta_c = 2500$ (left panel) and $\Delta_c = 500$ (right panel) for CSF clusters (red diamonds) and NR clusters (blue triangles).

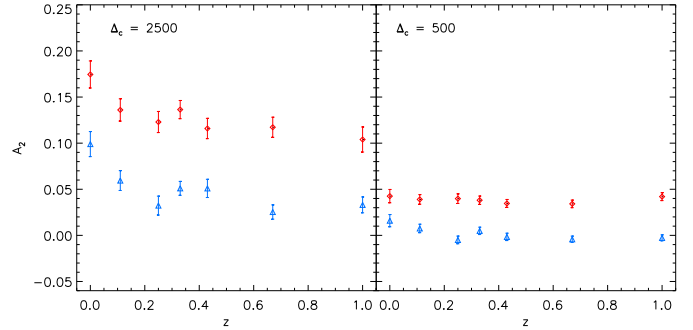


Figure 19. Same as Fig 18 but for the A_2 slope.

the average slopes, A_1 and A_2 , for CFS and NR clusters at two overdensities. In Fig. 20 we also show the dependence of the same slopes on overdensity for $z = 0$. As can be seen, there is a clear linear relation of A_1 and A_2 on Δ_c . We can therefore parametrize the variation of the slopes of the $Y f_{gas}^{-1} - M$ and $f_{gas} - M$ scaling relations expressed in equations 28 and 29 as follows:

$$A_1 = 1.64 - 0.65 \times \left(\frac{\Delta_c}{10^4} \right) \quad (34)$$

$$A_2 = 0.002 - 0.7 \times \left(\frac{\Delta_c}{10^4} \right) \quad (35)$$

Moreover, from the values of the best fit parameters listed in Table 3, the relation of the slopes for the different scaling relations expressed by Eq.(30) and Eq.(31), is confirmed by our clusters.

6 REDSHIFT EVOLUTION OF THE $Y - M$ SCALING RELATIONS

In the previous sections we have focused on the study of the $Y - M$ scaling relations from the MUSIC clusters at $z = 0$. In this section we will study the possible dependence of the SZ scaling relations with redshift.

We will employ two distinct approaches in our study:

- Selecting different complete volume limited samples above a given mass threshold for different redshift and repeating the study done at $z = 0$. This will give us the variations of the A and B best fit parameters of the $Y - M$ relation with redshift (Short et al. 2010; Fabjan et al. 2011; Kay et al. 2012). Following previous studies we can parametrize the redshift dependence as:

$$A(z) = A_0(1+z)^{\alpha_A} \quad (36)$$

$$B(z) = B_0(1+z)^{\alpha_B} \quad (37)$$

where A_0 and B_0 are the values of the slope at $z = 0$ and $\alpha_{A,B}$ the

	Δ_c (CSF)		$\Delta_b(z)$ (CSF)		Δ_c (NR)		$\Delta_b(z)$ (NR)	
	500	2500	1500(z)	7000(z)	500	2500	1500(z)	7000(z)
$\alpha_A(10^{-2})$	0.01 \pm 0.90	3.4 \pm 1.4	0.09 \pm 0.80	5.3 \pm 1.4	-1.7 \pm 1.4	1.6 \pm 1.0	-1.4 \pm 1.3	-1.6 \pm 0.8
$\alpha_B(10^{-2})$	0.07 \pm 0.80	2.7 \pm 1.1	1.3 \pm 0.7	4.5 \pm 1.2	-1.3 \pm 1.2	1.5 \pm 1.0	-0.3 \pm 1.1	-0.6 \pm 0.6

Table 4. Best fit parameters α_A , α_B of the evolution of A and B with redshift at different overdensities and physical processes.

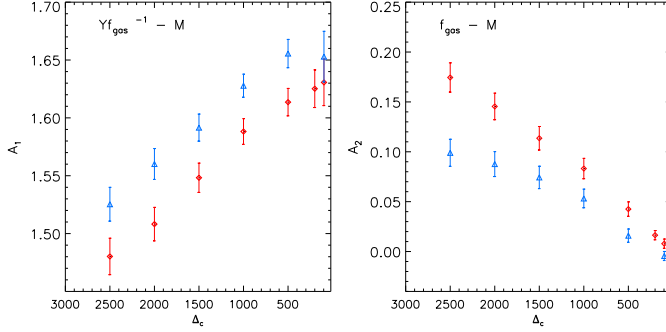


Figure 20. Left panel: the A_1 slope as a function of overdensity at $z = 0$ for CSF clusters (red diamonds) and NR clusters (blue triangles). Right panel: Same as left panel but for the A_2 slope.

best fit parameters that will describe the possible dependence with redshift.

- An alternative approach, more similar to observational studies, consisting of generating a sample of clusters that are carefully selected from different redshifts, by keeping the same proportion of abundance of clusters above a given mass at each redshift considered. From these samples, we look for possible dependence on redshift of the form:

$$Y f_{gas}^{-1} E(z)^{-2/3} = B M^A (1+z)^\beta \quad (38)$$

A similar approach has been adopted in Ferramacho & Blanchard (2011) with 438 clusters of the X-ray Galaxy Cluster Database (BAX) having redshifts ranging between 0.003 and 1 to obtain a large sample of potentially observable clusters in SZ.

Since we want to study the redshift evolution of the scaling relations for the two different definitions of aperture radius based on the overdensity criteria introduced in section 3 (and discussed in more detail in Appendix A), we have to make some preliminary considerations. When we use the redshift dependent background overdensity to define the integration area, we have to replace Δ_c in Eq. (17) of the $Y - M$ relation by:

$$\Delta_c = \Delta_b \cdot \left(\frac{\Delta_v(z)}{\Delta_v(0)} \right) \times \Omega_m(z). \quad (39)$$

In this case, the normalization parameter B is transformed as:

$$B = \log \frac{\sigma_T}{m_e c^2} \frac{\mu}{\mu_e} \left(\frac{\sqrt{\Delta_c} G H_0}{4} \right)^{2/3} + \log f_{gas} \left(\frac{\Delta_{b,v}(z)}{\Delta_{b,v}(0)} \Omega_m(z) \right)^{1/3} \quad (40)$$

But this introduces a natural evolution with redshift due to the scaling of $\Delta_b(z)$ that has to be subtracted from the fits to properly measure any intrinsic evolution of A and B .

z	0.00	0.11	0.25	0.33	0.43	0.67	1.00
N	271	237	187	147	117	44	8

Table 5. Number of MUSIC-2 clusters with $M_v > 5 \times 10^{14} h^{-1} M_\odot$ at different redshifts.

6.1 Evolution with redshift of the $Y - M$ best fit parameters

In Fig.21 we represent the mean values of the best fit A and B parameters of the complete volume limited mass samples for CSF clusters (upper panels) at the same four different overdensities already analyzed in section 3. We also estimated the scatter on $\sigma_{\log Y}$ for the same cases, calculated as in Eq.(25).

We can appreciate that the A slope and the normalization B show a clear evolution with redshift for low overdensities while they flat off when higher overdensity values are considered. The situation is the opposite when we consider higher overdensities: at these apertures the slope seems to be flatten off up to redshift $z \sim 0.5$ and then increases.

Table 4 shows the value of the best fit parameters α_A and α_B for the same overdensities analyzed in the previous sections. The results support the hypothesis of null evolution of $Y - M$ scaling relations at small overdensities ($\Delta_c=500$, $\Delta_b=1500(z)$) and a possible mild evolution at high overdensities ($\Delta_c=2500$, $\Delta_b=7000(z)$).

The total mass of the cluster seems to play a fundamental role in the evolution of the scaling relations. The same is also certain for the $f_{gas} - M$ scaling relation. The $Y - M$ relation seems therefore to satisfy self-similarity when considering massive evolved objects (we recall that all the clusters analyzed in this paper have $M_v > 5 \times 10^{14} h^{-1}$ at $z=0$). When smaller mass systems are added to the catalogues, the deviations from self-similarity become more apparent, as it is clearly shown in Table. 4

The rms scatter of $\log_{10} Y$, $\sigma_{\log Y}$, is also shown in the lower row of the upper panel of Fig.21. Although it is nearly constant at low overdensities (about 4 per cent), its value increases (from 6 per cent to 8 per cent) at high overdensities and high redshifts.

If we look at the same evolution in NR clusters (bottom panels of Fig.21), we find that, in this case, there is no evidence of any change in the slope with redshift, and the values of α_A and α_B are extremely low at all overdensities (Table 4). Also the scatter is small (never exceeding 4 per cent) and does not vary with redshift.

From Fig.21 and Table 4 we can also conclude that the evolution of A and B is not affected by the choice of the overdensity (fixed critical or redshift dependent background), since both methods lead to the same results (evolution at high overdensities and smaller masses for CSF clusters and no significant evolution for NR clusters). Therefore, there is no need to change from the widely used, and more simple, assumption of a fixed critical overdensity to define the aperture radius.

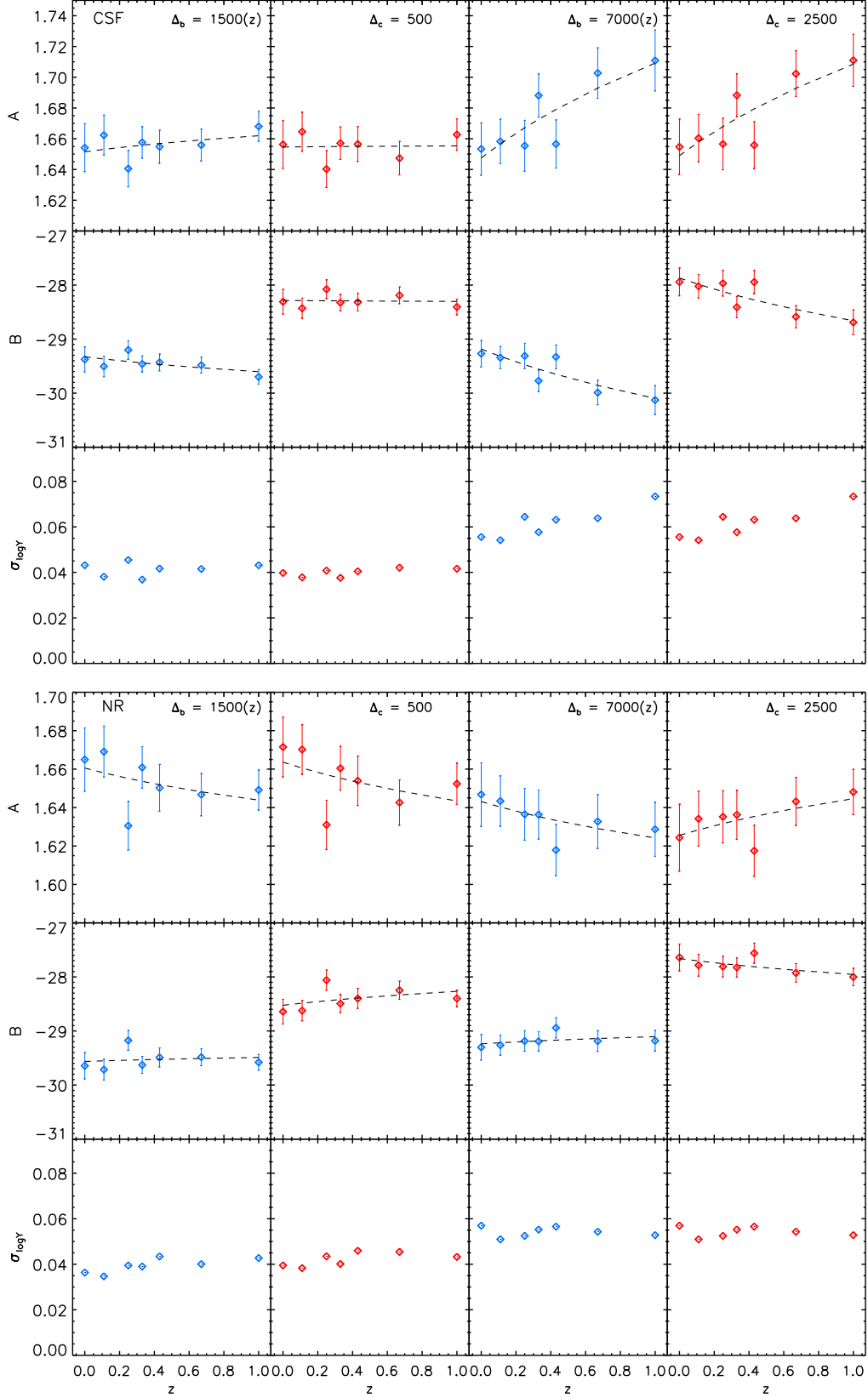


Figure 21. Evolution with redshift of the slope (top panels), of the normalization (central panels) and of the scatter (bottom panels). The upper part (first three rows) of the figure describe CSF clusters, the lower (last three rows) the NR clusters. Redshift varying background density (blue diamonds) at $\Delta_b=1500(z)$ (left) and $\Delta_b=7000(z)$ (right) and fixed critical overdensity (red diamonds) at $\Delta_c=500$ (left) and $\Delta_c=2500$ (right).

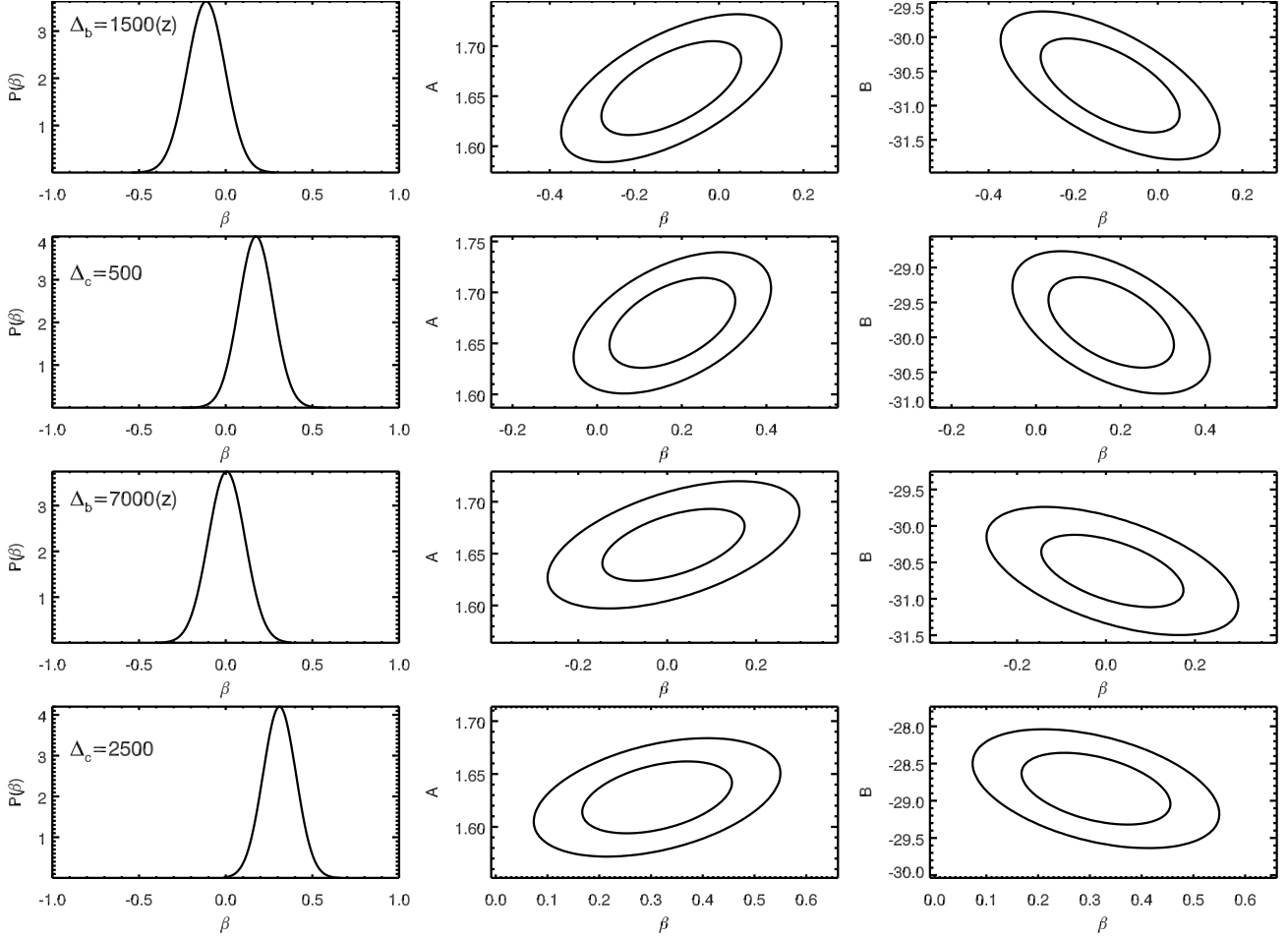


Figure 22. Posterior distributions for the β parameter at the 4 overdensities considered: $\Delta_b=1500(z)$, $\Delta_c=500$, $\Delta_b=7000(z)$, $\Delta_c=2500$. The contours correspond to 1 and 2 σ intervals for the best fit parameters.

6.2 Mixed-z sample results

As we said above, we have also checked the evolution of the $Y - M$ scaling relation on mixed- z datasets to mimic the variety of clusters that should populate an observational mass-limited galaxy cluster survey. These datasets have been built by selecting subsamples of CSF objects from all the available redshifts, with the prescription that every member appears in the sample only at one redshift and that the sample is populated according to the cluster abundances of MUSIC-2 as a function of redshift (see Table 5). This approach allows us to evaluate systematics in the reconstruction of the $Y - M$ scaling relation. Moreover, if some evolution or mass dependence actually exists, it will also help us to estimate the level at which it is detectable in a complete mass-limited cluster sample

We assume Eq.(38) as our reference scaling law:

$$\log(YE(z)^{-2/3}f_{gas}^{-1}) = B + A \log M + \beta \log(1+z) \quad (41)$$

The fit has been performed with a standard Monte Carlo Markov Chain algorithm based on the Metropolis-Hastings sampling scheme, where no additional priors have been applied on the slope parameter. The convergence has been assessed through the Gelman-Rubin test (Gelman & Rubin 1992) on a set of three simultaneous chains run on the same dataset from independent starting points in parameter space. The samples were drawn at the four reference overdensities (again $\Delta_c = 2500$, 500 and $\Delta_b(z)=7000(z)$,

	$\Delta_c=500$	$\Delta_c=2500$	$\Delta_b = 1500(z)$	$\Delta_b = 7000(z)$
A	1.672 ± 0.028	1.627 ± 0.022	1.652 ± 0.028	1.656 ± 0.023
B	-29.77 ± 0.42	-28.85 ± 0.32	-30.65 ± 0.42	-30.61 ± 0.33
β	0.17 ± 0.10	0.31 ± 0.14	-0.12 ± 0.11	0.00 ± 0.11

Table 6. Best fit parameters (slope A, normalization B and redshift evolution β) for the $Y - M$ scaling relation on a mixed- z sample of 250 CSF clusters.

1500(z)). Fig. 22 shows the posterior distributions of β and the $\beta - A$ and $\beta - B$ joint likelihoods for the reference overdensities. The fit results are still fairly consistent with self similarity and no additional redshift scaling in the $Y - M$ scaling relation, except for the $\Delta_c = 2500$ dataset, which shows marginal evidence of residual scaling. Since the mixed- z cluster sample has been drawn from the original simulated dataset randomly, the procedure was iterated on 5000 samples to check for the possibility of large fluctuations in the fit results (e.g. due to outliers in the data distribution). This was not the case, since the best-fit parameters at the 4 overdensities lied well within the range of fluctuation allowed by the individual-sample posterior distributions. In Table 6 all the 3 best fit parameters are listed with their corresponding 1 σ errors. The $Y - M$ scaling laws for one realization of a mixed- z sample and only for low overdensities, are plotted in Figs. 23 and 24.

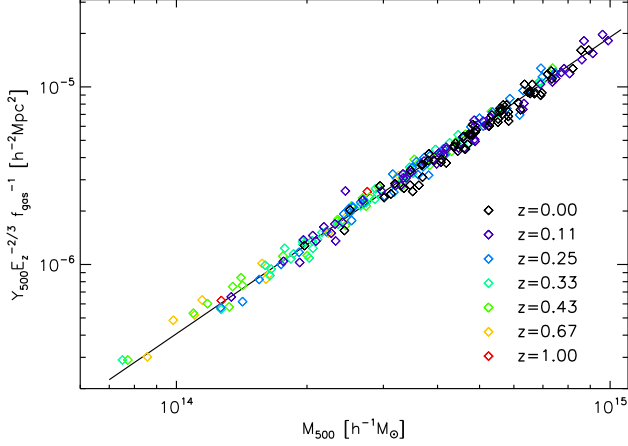


Figure 23. Mixed- z scaling relation at $\Delta_c = 500$; the different diamond colors refer to different redshifts between $z = 0$ and $z = 1$.

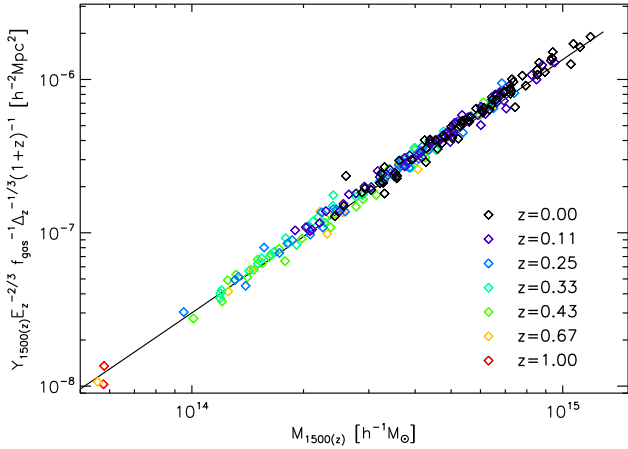


Figure 24. Mixed- z scaling relation at $\Delta_b = 1500(z)$; the different diamond colors refer to different redshifts between $z = 0$ and $z = 1$.

7 SUMMARY AND CONCLUSIONS

Recent new large scale surveys on the far infrared and millimeter bands confirmed the validity of the Sunyaev-Zel'dovich Effect as a useful cosmological tool to detect and to study galaxy clusters. Today, one of its most relevant applications is to infer the total cluster mass using the $Y - M$ scaling relation. Recent observations (Planck, SPT and ACT) provide the SZ-measurements of a large number of clusters from which the $Y - M$ relation can be reliably inferred.

In this paper we have presented the MUSIC dataset, a large sample of gasdynamical resimulated massive clusters, that have been selected from the MareNostrum Universe simulation and from the MultiDark simulation. Our dataset comprises two different subsamples. The MUSIC-1 which contains 164 objects that have been selected according to their dynamical state (i.e. bullet-like clusters and relaxed clusters) and the MUSIC-2 which contains a total of more than 2000 galaxy groups and clusters. The MUSIC-2 constitutes a complete volume limited sample for clusters with virial masses above $8 \times 10^{14} h^{-1} M_{\odot}$ at $z = 0$. To our knowledge, there are no other works about resimulated clusters that have shown such

a large number of massive objects. These objects have been simulated using two physical processes: non-radiative (NR, gravitational heating only) and a radiative model (CSF) including cooling, UV photoionisation, multiphase ISM and star formation and supernovae feedbacks. No AGN feedback has been included in the radiative simulations.

We plan to generate mock catalogues from the MUSIC clusters for the most common observables such as: X-ray and SZE surface brightness maps, lensing maps and galaxy luminosity functions. All these deliverables, together with the initial conditions for all the MUSIC simulations, will be made publicly available from the website <http://music.ft.uam.es>.

Here we have presented the first results from MUSIC based on the analysis of the baryon content and the scaling relations of the thermal SZ effect.

The analysis of the integrated cluster quantities, such as the fractions of the different baryon components, or Y parameter, have been done using two definitions of the aperture radius. The most commonly used approach assumes that the integration domain is defined by a fixed value of the mean overdensity inside the cluster region compared to the critical overdensity of the Universe. It has been shown (see Appendix A) that this definition introduces a bias when any integrated quantity is compared at different redshifts. On the contrary, by using a redshift-dependent overdensity compared to the background density of the Universe we can rescale the aperture radius such that the integrated region is always the same volume fraction of the total cluster volume defined by the virial radius.

Our numerical results on the baryon content and the SZ scaling relations have been explored to check possible dependences on overdensity, redshift and cluster physics modelling. We have also made a comparison between MUSIC clusters and available observational results. The scaling relation between SZ brightness, quantified with the integrated Compton y -parameter, Y , and the cluster total mass, M , confirmed the robustness of the self-similarity assumption for this class of objects present in MUSIC sample. We evaluated the effect on the $Y - M$ of having the cluster gas fraction, f_{gas} , as a free parameter that can vary with the cluster mass. Finally, we looked for a possible redshift evolution of the $Y - M$ relation using two different approaches.

Our main conclusions can be summarized as follows:

- The mean value of the gas fraction of MUSIC-2 CSF clusters at $\Delta_c=500$ is $f_{gas}=0.118 \pm 0.005$. This value is compatible with observational results shown in Maughan et al. (2004), LaRoque et al. (2006), Maughan et al. (2006), Vikhlinin et al. (2009), Zhang et al. (2010), Ettori et al. (2009), Juett et al. (2010), and David et al. (2012). The values of the baryon fraction at virial radius, for both simulation flavours (CSF and NR), are consistent, within the errors, with the cosmological ratio Ω_b/Ω_m (according to WMAP7 cosmology). At higher overdensities (i.e. $\Delta_c=2500$), we also find agreement for the f_{gas} with observational results from Maughan et al. (2006), Vikhlinin et al. (2009) and Zhang et al. (2010) and we are marginally consistent with Allen et al. (2008) and David et al. (2012). This means that the possible effects of numerical overcooling do not appear to affect dramatically our simulations, despite the fact that we have not included strong AGN feedback in our model. Concerning the evolution with redshift of the different baryon components, we find significant differences in the evolution depending on the definition of aperture radius used. This is more evident at large overdensities, where the considered fraction of virial radius increases with redshift when a fixed critical overdensity is used to define it (see Fig. A1).

• The $Y - M$ scaling relation derived from our clusters, assuming a fixed f_{gas} , agrees very well with the predictions of the self-similar model and shows a very low dispersion ($\sigma_{\log Y} \simeq 0.04$). The resulting best fit $Y_{500} - M_{500}$ relation can then be expressed as:

$$Y_{500} = 10^{-28.3 \pm 0.2} \left(\frac{M_{500}}{h^{-1} M_{\odot}} \right)^{1.66 \pm 0.02} E(z)^{-2/3} [h^{-2} Mpc^2] \quad (42)$$

The $M - Y$ relation, which is more suitable to infer cluster masses from Y measurements, is also compatible with the self-similar model (which predicts a slope of 3/5) with an even lower dispersion ($\sigma_{\log M} \simeq 0.03$). The corresponding best-fit $M_{500} - Y_{500}$ relation can be expressed as:

$$M_{500} = 10^{17.0 \pm 0.1} \left(\frac{Y_{500}}{h^{-2} Mpc^2} \right)^{0.59 \pm 0.01} E(z)^{-2/5} [h^{-1} M_{\odot}] \quad (43)$$

We have compared the above fits with the recent results on the $Y - M$ from the Planck Collaboration. The agreement is very good, provided that the masses of Planck clusters are overestimated by 22 per cent due to the biases of the X-ray mass estimations with respect to the lensing measurements. We have tested whether this bias could be due to the lack of hydrostatic equilibrium hypothesis. By comparing the hydrostatic masses with the true one in our MUSIC samples, we find a negative HMB (an opposite trend than in Planck clusters). In our case, we find 25 per cent underestimation of the true mass by the hydrostatic mass.

• The dependence of the gas fraction on the cluster total mass has been also studied along the cluster aperture radius. There is a linear relation between f_{gas} and total mass which is more evident, although with larger scatter, when we approach the cluster core. This effect is rather insensitive on the adopted physics in the numerical simulations: both CSF and NR clusters present a similar behaviour.

• Leaving f_{gas} as a free parameter in the $Y - M$ scaling relation leads to a deviation from self-similarity. The modified $Y f_{gas}^{-1} - M$ relation and the $f_{gas} - M$ relation are directly related with the $Y - M$ if both of them are expressed as power laws. We confirm this hypothesis and provide the fits to the $f_{gas} - M$ for two overdensities $\Delta_c = 2500$ and $\Delta_c = 500$

$$f_{gas} = 10^{-3.5 \pm 0.2} \left(\frac{M_{2500}}{h^{-1} M_{\odot}} \right)^{0.17 \pm 0.01} \quad (44)$$

$$f_{gas} = 10^{-1.6 \pm 0.1} \left(\frac{M_{500}}{h^{-1} M_{\odot}} \right)^{0.04 \pm 0.01} \quad (45)$$

• We have studied the redshift evolution of the slope, and of the normalization, in the $Y - M$ scaling law. We did not find any evolution for NR clusters. On the contrary, CSF clusters show a marginal deviation of the slope from the self-similar prediction at high overdensity for redshifts larger than 0.5. This result is confirmed using two different methods to study the evolution with redshift.

• No significant differences have been found when comparing results at different redshifts using the two alternative definitions of aperture areas based on different overdensity criteria: the standard, redshift independent, critical overdensity and the redshift-dependent background overdensity show the same results, at least for the gas fraction analysis, with the latter appearing to be more sensitive to the redshift evolution of the sample properties ($Y - M$ slope, gas fraction, etc.). We can therefore conclude that even if the redshift-dependent background overdensity leads to results which better identify a possible evolution, no significant errors are introduced in the analysis of the SZ effects when using the standard

critical overdensity criteria. The same conclusions in the case of X-ray analyzes have been raised by Maughan et al. (2006).

• The use of radiative physics on galaxy cluster simulations introduces fundamental improvements respect to non-radiative simulations: CSF clusters show better agreement with observations in the estimate of the gas fraction as well as in the study of the $Y - M$ scaling relation. On the other hand, NR clusters overestimate the gas fraction and do not seem to be compatible with $Y - M$ scaling relations from observational results.

In summary, we have shown that the MUSIC dataset is well suited for the study of massive cluster properties and provides a reasonable description of observed objects with similar mass. Therefore, the MUSIC clusters can be a good cosmological tool. In upcoming papers we are going to extend the analysis to other complementary scaling relations in X-ray, lensing and optical in order to have a full set of observables for a complete volume limited sample of Λ CDM simulated galaxy clusters.

APPENDIX A: CLUSTER APERTURE RADIUS DEFINITIONS

A correct analysis of the integrated properties of clusters at similar or different redshift, is based on the definition of the aperture radius. Ideally the virial radius is a suitable choice, confining almost the whole cluster. Unfortunately a such large region is challenging to be explored due to the lack of sensitivity of present day SZ or X-ray observations. Therefore, a smaller aperture radius has to be defined. This quantity has to be physically meaningful and must hold at different redshifts.

The widely applied definition of the aperture radius, both in observations and simulations, correspond to the radius of a sphere that contains a total mass that equals the mass of a sphere with a fixed redshift independent overdensity with respect to the critical density defined as

$$\rho_c(z) = \frac{3H_0^2 E(z)^2}{8\pi G} \quad (A1)$$

where H_0 is the present value of the Hubble constant, G is the universal gravitational constant.

An alternative definition of the aperture radius consists in defining it as the radius of the sphere that contains a total mass equal to the mass of a sphere with an overdensity value with respect to the cosmic background mass density, $\rho_b(z) = \rho_c(z)\Omega_m(z)$ where $\Omega_m(z)$ is the cosmological matter density parameter defined as $\Omega_m(z) = \Omega_M(1+z)^3/E^2(z)$.

The cluster centric radius can then be quantified in terms of these two overdensities $\Delta_{b,c}$, which means that the cluster average density inside $r_{\Delta_{b,c}}$ is Δ times the critical or background density. The overdensity radius, linked to the critical (or background) density, can therefore be expressed as:

$$r_{\Delta_c} = \left(\frac{3M_{\Delta_c}(z)}{4\pi\rho_c(z)\Delta_c(z)} \right)^{1/3} \quad (A2)$$

$$r_{\Delta_b} = \left(\frac{3M_{\Delta_b}(z)\Omega_m(z)}{4\pi\rho_c(z)\Delta_b(z)} \right)^{1/3} \quad (A3)$$

It is important to check whether a redshift independent Δ_c could possibly introduce some biases when comparing clusters at different redshifts. Our goal is to keep the ratio r/R_v constant with redshift so that the same fraction of cluster is considered at different redshifts.

Maughan et al. (2006) were the first to address this problem. They investigated the influence of the definition of overdensity radius only in the case of X-ray scaling relations with a sample of 11 high-redshift clusters observed with Chandra and/or XMM-Newton. Also recently a study of scaling laws specifically, for X-ray observables and cluster properties, has faced the same problem (Böhringer et al. 2012).

The dependence of the overdensity radius defined in Eq.A2 on redshift and on cosmological parameters can be easily derived:

$$r_{\Delta_c} \propto \rho_c(z)^{-1/3} \propto E^{-2/3}(z) = (\Omega_M(1+z)^3 + \Omega_\Lambda)^{-1/3} \quad (\text{A4})$$

Similarly, the radius defined with the background overdensity depends on redshift as

$$r_{\Delta_b} \propto \rho_c(z)^{-1/3} \Omega_m(z)^{-1/3} \propto (1+z)^{-1} \quad (\text{A5})$$

As can be seen, the dependence on redshift of the two defined radius is somewhat different. From $z = 0$ to $z = 1$, the r_{Δ_c} decreases by a factor of 1.4 while the r_{Δ_b} decreases a factor of 2. But, we are interested to check how the ratio $r_{\Delta_{c,b}}/R_v$ depends on redshift. Thus, we take into account the dependence of the overdensity at virial radius R_v , Δ_v . An analytical fit to the numerical solution of the spherical collapse model was given by Bryan & Norman (1998) in a Λ CDM cosmology (see also Eke et al. (1996)).

$$\Delta_{v,c}(z) \sim 18\pi^2 + 82x - 39x^2 \quad (\text{A6})$$

as to the background density, is given by:

$$\Delta_{v,b}(z) \sim \Delta_{v,c}(z)/(1+x) \quad (\text{A7})$$

where $x = \Omega_m(z) - 1$.

With this definition of aperture radius the r_{Δ_c}/R_v ratio changes with redshift as it is shown in right panel of Fig. A1. The effect increases towards the inner regions of the cluster. An overdensity radius of 2500 over the critical density corresponds to a region of 1/5th of the virial radius at $z = 0$ and changes by more than 20 per cent towards $z = 1$.

Maughan et al. (2006) suggested an alternative definition of aperture radius to show an almost redshift independent variation of r/R_v . To this end, they propose to define the aperture radius with a redshift dependent overdensity value which is a simple rescaling of the overdensity defined at $z = 0$ as:

$$\Delta(z) = \Delta(0) \left[\frac{\Delta_v(z)}{\Delta_v(0)} \right] \quad (\text{A8})$$

In this way, the ratio of the comoving densities is ensured to be constant along the redshift. We refer to this redshift varying overdensity as $\Delta(z)$, following the notation adopted by Maughan et al. (2006).

By looking at the dependence on redshift, cosmology and on the density contrast at the virial radius, a background overdensity, including the z -dependence (Eq.A8), seems to be a more suitable choice for the Δ definition, allowing to compare cluster properties within radii corresponding to redshift independent cluster fractions. In fact, as can be seen in the left panel of Fig. A1 $r_{\Delta_b(z)}/R_v$, estimated from the redshift dependent background overdensity, $\Delta_b(z)$, looks almost invariant with redshift (less than 5 per cent variation). Thus, applying this definition, we will be able to study the evolution of cluster properties almost free from the bias induced by the choice of an aperture radius defined by the same overdensity value at all redshifts.

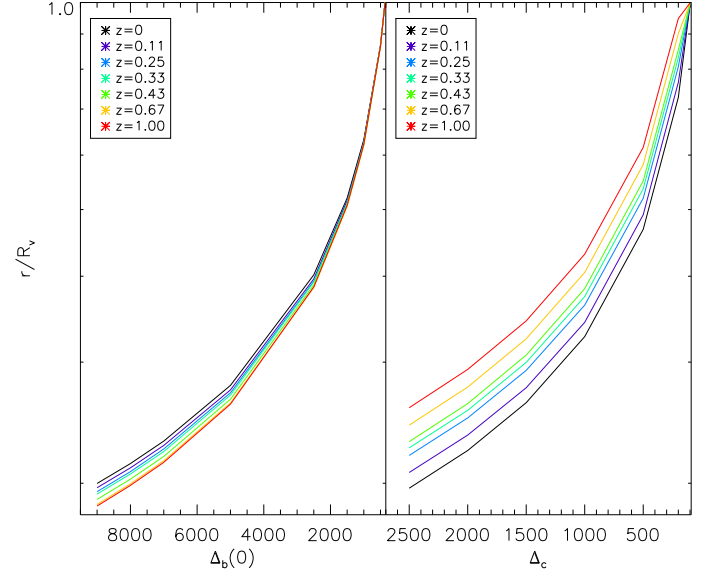


Figure A1. Behaviour of the r/R_v ratio at different redshifts ($0 \leq z \leq 1$) for background overdensity varying with redshift (left panel) and for fixed critical overdensity (right panel).

ACKNOWLEDGEMENTS

The MUSIC simulations were performed at the Barcelona Supercomputing Center (BSC) and the initial conditions were done at the Leibniz Rechenzentrum Munich (LRZ). We thank the support of the MICINN Consolider-Ingenio 2010 Programme under grant MultiDark CSD2009-00064. GY acknowledges support from MICINN under research grants AYA2009-13875-C03-02, FPA2009-08958 and Consolider Ingenio SyeC CSD2007-0050. FS, MDP, LL and BC have been supported by funding from the University of Rome 'Sapienza', Anno 2011 - prot. C26A11BYBF. FS is also supported by the Spanish Ministerio de Ciencia e Innovación (MICINN) with a FPU fellowship. MDP wish to thank the Ministerio de Educacion, Cultura y Deporte for supporting his visit at UAM during the final phase of preparation of this paper.

REFERENCES

- Aghanim N., da Silva A. C., Nunes N. J., 2009, *A&A*, 496, 637
- Allen S. W., Rapetti D. A., Schmidt R. W., Ebeling H., Morris R. G., Fabian A. C., 2008, *MNRAS*, 383, 879
- Ameglio S., Borgani S., Pierpaoli E., Dolag K., Ettori S., Morandi A., 2009, *MNRAS*, 394, 479
- Andersson K. et al., 2011, *ApJ*, 738, 48
- Andersson K., SPT Collaboration, 2010, in *AAS/High Energy Astrophysics Division*, Vol. 11, *AAS/High Energy Astrophysics Division 11*, p. 27.04
- Arnaud M., Pratt G. W., Piffaretti R., Böhringer H., Croston J. H., Pointecouteau E., 2010, *A&A*, 517, A92
- Battaglia N., Bond J. R., Pfrommer C., Sievers J. L., 2011, *ArXiv e-prints* 1109.3709B
- Benson B. A., Church S. E., Ade P. A. R., Bock J. J., Ganga K. M., Henson C. N., Thompson K. L., 2004, *ApJ*, 617, 829
- Biffi V., Dolag K., Böhringer H., Lemson G., 2012, *MNRAS*, 420, 3545
- Böhringer H., Dolag K., Chon G., 2012, *A&A*, 539, A120

- Bonaldi A., Tormen G., Dolag K., Moscardini L., 2007, *MNRAS*, 378, 1248
- Bonamente M., Joy M., LaRoque S. J., Carlstrom J. E., Nagai D., Marrone D. P., 2008, *ApJ*, 675, 106
- Borgani S., Kravtsov A., 2009, *ArXiv e-prints* 2009arXiv0906.4370B
- Borgani S. et al., 2004, *MNRAS*, 348, 1078
- Boylan-Kolchin M., Springel V., White S. D. M., Jenkins A., Lemson G., 2009, *MNRAS*, 398, 1150
- Browne I. W., Mao S., Wilkinson P. N., Kus A. J., Marecki A., Birkinshaw M., 2000, in *Society of Photo-Optical Instrumentation Engineers (SPIE) Conference Series*, Butcher H. R., ed., Vol. 4015, pp. 299–307
- Bryan G. L., Norman M. L., 1998, *ApJ*, 495, 80
- Burns J. O., Hallman E. J., Gantner B., Motl P. M., Norman M. L., 2008, *ApJ*, 675, 1125
- Clowe D., Bradač M., Gonzalez A. H., Markevitch M., Randall S. W., Jones C., Zaritsky D., 2006, *ApJ*, 648, L109
- Comis B., De Petris M., Conte A., Lamagna L., De Gregori S., 2011, *MNRAS*, 418, 1089
- Cooray A. R., Carlstrom J. E., Grego L., Holder G. P., Holzapfel W. L., Joy M., Patel S. K., Reese E., 1999, in *American Institute of Physics Conference Series*, Vol. 470, *After the Dark Ages: When Galaxies were Young*, S. Holt & E. Smith, ed., pp. 184–187
- Croston J. H. et al., 2008, *A&A*, 487, 431
- da Silva A. C., Barbosa D., Liddle A. R., Thomas P. A., 2000, *MNRAS*, 317, 37
- da Silva A. C., Kay S. T., Liddle A. R., Thomas P. A., 2004, *MNRAS*, 348, 1401
- David L. P., Jones C., Forman W., 2012, *ApJ*, 748, 120
- De Petris M. et al., 2007, *New Astron. Rev.*, 51, 368
- Devriendt J. E. G., Guiderdoni B., Sadat R., 1999, *A&A*, 350, 381
- Dolag K., Borgani S., Murante G., Springel V., 2009, *MNRAS*, 399, 497
- Dolag K., Reinecke M., Gheller C., Imboden S., 2008, *New Journal of Physics*, 10, 125006
- Eke V. R., Cole S., Frenk C. S., 1996, *MNRAS*, 282, 263
- Ettori S., Morandi A., Tozzi P., Balestra I., Borgani S., Rosati P., Lovisari L., Terenziani F., 2009, *A&A*, 501, 61
- Ettori S., Tozzi P., Borgani S., Rosati P., 2004, *A&A*, 417, 13
- Fabjan D., Borgani S., Rasia E., Bonafede A., Dolag K., Murante G., Tornatore L., 2011, *MNRAS*, 416, 801
- Fabjan D., Borgani S., Tornatore L., Saro A., Murante G., Dolag K., 2010, *MNRAS*, 401, 1670
- Ferramacho L. D., Blanchard A., 2011, *A&A*, 533, A45
- Flores-Cacho I. et al., 2009, *MNRAS*, 400, 1868
- Forero-Romero J. E., Gottlöber S., Yepes G., 2010, *ApJ*, 725, 598
- Gardini A., Rasia E., Mazzotta P., Tormen G., De Grandi S., Moscardini L., 2004, *MNRAS*, 351, 505
- Gelman A., Rubin D., 1992, *Statistical Science*, 7, 457
- Golwala S. R. et al., 2007, in *Bulletin of the American Astronomical Society*, Vol. 38, *American Astronomical Society Meeting Abstracts*, p. 886
- Gottlöber S., Yepes G., 2007, *ApJ*, 664, 117
- Hallman E. J., O'Shea B. W., Burns J. O., Norman M. L., Harkness R., Wagner R., 2007, *ApJ*, 671, 27
- Hartley W. G., Gazzola L., Pearce F. R., Kay S. T., Thomas P. A., 2008, *MNRAS*, 386, 2015
- Juett A. M., Davis D. S., Mushotzky R., 2010, *ApJ*, 709, L103
- Kaiser N., 1986, *MNRAS*, 222, 323
- Kay S. T., da Silva A. C., Aghanim N., Blanchard A., Liddle A. R., Puget J.-L., Sadat R., Thomas P. A., 2007, *MNRAS*, 377, 317
- Kay S. T., Peel M. W., Short C. J., Thomas P. A., Young O. E., Battye R. A., Liddle A. R., Pearce F. R., 2012, *MNRAS*, 2792
- Klypin A., Kravtsov A. V., Bullock J. S., Primack J. R., 2001, *ApJ*, 554, 903
- Knebe A. et al., 2011, *MNRAS*, 415, 2293
- Knollmann S. R., Knebe A., 2009, *ApJS*, 182, 608
- Komatsu E. et al., 2011, *ApJS*, 192, 18
- Korngut P. M. et al., 2011, *ApJ*, 734, 10
- Krause E., Pierpaoli E., Dolag K., Borgani S., 2012, *MNRAS*, 419, 1766
- Kravtsov A. V., Klypin A. A., Khokhlov A. M., 1997, *ApJS*, 111, 73
- Kravtsov A. V., Nagai D., Vikhlinin A. A., 2005, *ApJ*, 625, 588
- Kravtsov A. V., Vikhlinin A., Nagai D., 2006, *ApJ*, 650, 128
- LaRoque S. J., Bonamente M., Carlstrom J. E., Joy M. K., Nagai D., Reese E. D., Dawson K. S., 2006, *ApJ*, 652, 917
- Lau E. T., Kravtsov A. V., Nagai D., 2009, *ApJ*, 705, 1129
- Leccardi A., Molendi S., 2008, *A&A*, 486, 359
- Lo K., Martin R., Chiueh T., 2001, in *2001 Asia-Pacific Radio Science Conference AP-RASC '01*, p. 235
- Loken C., Norman M. L., Nelson E., Burns J., Bryan G. L., Motl P., 2002, *ApJ*, 579, 571
- Marriage T. A. et al., 2011, *ApJ*, 737, 61
- Masi S. et al., 2008, *Mem. Soc. Astron. Italiana*, 79, 887
- Mastropietro C., Burkert A., 2008, *MNRAS*, 389, 967
- Maughan B. J., Jones L. R., Ebeling H., Scharf C., 2004, *MNRAS*, 351, 1193
- Maughan B. J., Jones L. R., Ebeling H., Scharf C., 2006, *MNRAS*, 365, 509
- Mazzotta P., Rasia E., Moscardini L., Tormen G., 2004, *MNRAS*, 354, 10
- McCarthy I. G., Babul A., Holder G. P., Balogh M. L., 2003, *ApJ*, 591, 515
- Morandi A., Ettori S., Moscardini L., 2007, *MNRAS*, 379, 518
- Motl P. M., Hallman E. J., Burns J. O., Norman M. L., 2005, *ApJ*, 623, L63
- Mroczkowski T. et al., 2009, *ApJ*, 694, 1034
- Muanwong O., Kay S. T., Thomas P. A., 2006, *ApJ*, 649, 640
- Muchovej S., Leitch E., Culverhouse T., Carpenter J., Sievers J., 2012, *ApJ*, 749, 46
- Nagai D., 2006, *ApJ*, 650, 538
- Nagai D., Kravtsov A. V., Vikhlinin A., 2007a, *ApJ*, 668, 1
- Nagai D., Vikhlinin A., Kravtsov A. V., 2007b, *ApJ*, 655, 98
- Piffaretti R., Valdarnini R., 2008, *A&A*, 491, 71
- Planck Collaboration et al., 2011a, *A&A*, 536, A8
- Planck Collaboration et al., 2011b, *A&A*, 536, A11
- Planck Collaboration et al., 2012, *arXiv:1204.2743v1*
- Planck Collaboration et al., 2011c, *A&A*, 536, A10
- Planck Collaboration et al., 2011d, *A&A*, 536, A12
- Poole G. B., Babul A., McCarthy I. G., Fardal M. A., Bildfell C. J., Quinn T., Mahdavi A., 2007, *MNRAS*, 380, 437
- Prada F., Klypin A. A., Cuesta A. J., Betancort-Rijo J. E., Primack J., 2011, *arXiv:1104.5130v1*
- Puchwein E., Sijacki D., Springel V., 2008, *ApJ*, 687, L53
- Rasia E. et al., 2006, in *EAS Publications Series*, Vol. 20, *EAS Publications Series*, Mamon G. A., Combes F., Deffayet C., Fort B., eds., pp. 295–296
- Rasia E., Mazzotta P., Bourdin H., Borgani S., Tornatore L., Ettori S., Dolag K., Moscardini L., 2008, *ApJ*, 674, 728
- Roncarelli M., Ettori S., Dolag K., Moscardini L., Borgani S., Murante G., 2006, *MNRAS*, 373, 1339

- Sehgal N. et al., 2011, ApJ, 732, 44
Short C. J., Thomas P. A., Young O. E., Pearce F. R., Jenkins A.,
Muanwong O., 2010, MNRAS, 408, 2213
Springel V., 2005, MNRAS, 364, 1105
Springel V., Farrar G. R., 2007, MNRAS, 380, 911
Springel V., Hernquist L., 2003, MNRAS, 339, 289
Staniszewski Z. et al., 2009, ApJ, 701, 32
Sunyaev R. A., Zeldovich Y. B., 1970, Ap&SS, 7, 3
Vanderlinde K. et al., 2010, ApJ, 722, 1180
Vikhlinin A. et al., 2009, ApJ, 692, 1033
Vikhlinin A., Kravtsov A., Forman W., Jones C., Markevitch M.,
Murray S. S., Van Speybroeck L., 2006, ApJ, 640, 691
White M., Hernquist L., Springel V., 2002, ApJ, 579, 16
Wik D. R., Sarazin C. L., Ricker P. M., Randall S. W., 2008, ApJ,
680, 17
Williamson R. et al., 2011, ApJ, 738, 139
Yang H.-Y. K., Bhattacharya S., Ricker P. M., 2010, ApJ, 725,
1124
Zhang Y.-Y. et al., 2010, ApJ, 711, 1033
Zwart J. T. L. et al., 2008, MNRAS, 391, 1545

This paper has been typeset from a \TeX / \LaTeX file prepared by the author.